Energy & Environmental Science

REVIEW

View Article Online
View Journal | View Issue

Cite this: *Energy Environ. Sci.*, 2014, **7**, 1564

A review of graphene and graphene oxide sponge: material synthesis and applications to energy and the environment

Victor Chabot,[a] Drew Higgins,[a] Aiping Yu,*[a] Xingcheng Xiao,[b] Zhongwei Chen[a] and Jiujun Zhang*[c]

Received 11th October 2013
Accepted 11th February 2014

DOI: 10.1039/c3ee43385d

www.rsc.org/ees

This paper gives a comprehensive review about the most recent progress in synthesis, characterization, fundamental understanding, and the performance of graphene and graphene oxide sponges. Practical applications are considered including use in composite materials, as the electrode materials for electrochemical sensors, as absorbers for both gases and liquids, and as electrode materials for devices involved in electrochemical energy storage and conversion. Several advantages of both graphene and graphene oxide sponges such as three dimensional graphene networks, high surface area, high electro/thermo conductivities, high chemical/electrochemical stability, high flexibility and elasticity, and extremely high surface hydrophobicity are emphasized. To facilitate further research and development, the technical challenges are discussed, and several future research directions are also suggested in this paper.

Broader context

Advanced graphene materials residing at the frontier of scientific research offer immense potential for overcoming the challenges related to the performance, functionality and durability of key functional materials' in the fields of life science, energy, and the environment. Future demand necessitates advanced processing methods be developed that can mass produce high quality, two-dimensional graphene sheets while overcoming the issues of poor dispersion and restacking with large size-scale deployment of two-dimensional graphene sheets. These issues, along with graphene sheet defects and multilayer thicknesses prevent the full realization of graphene's high potential, including electronic properties and high surface area. Three-dimensional arrangements have been recently able to address these limitations, by creating sponge-like low density materials with a long list of beneficial properties including: macroscale size, high accessible surface area, less restacking, highly-interconnected microstructure, high strength and flexibility, fast ion transport and electron conductivity. This review is intended to address the continued developments and challenges with a wide scope of interest, highlighting fundamental understanding of the synthesis and characterization procedures, future outlook, as well as an in-depth discussion of application areas reporting high performance in recent publications. The outstanding potential of these materials has enabled significant enhancements for numerous important applications such as electrochemical energy storage and conversion, absorption, sensing, catalysis, transistors and polymer composites.

1 Introduction

In today's world, frontier scientific and technological research into the fields of life science, energy, as well as the environment is facing challenges with the performance, functionality and durability of key materials. It has been widely recognized that advanced materials including carbon-based nano-materials such as active carbon (carbon black), carbon nanotubes, carbon nanofibers, graphene and so on will continue to play a more and more important role in the effort to overcome the major challenges and make breakthroughs in both technology and in practical application. These advanced carbon nano-materials have been and will continue to be widely employed in various important applications such as electrochemical energy storage and conversion, sensing, catalysis, transistors and polymer composites.[1–10]

Graphene, as one of these advanced carbon nano-materials, is a 2-dimensional single sheet of carbon atoms arranged in a hexagonal network. It was discovered in 2004 through a process of scotch tape peeling.[11] The ideal graphene sheets that can be achieved by this mechanical exfoliation technique have proven to be: highly ordered, exhibit outstanding surface areas (2630 $m^2\ g^{-1}$), high Young's modulus (1 TPa), high thermal conductivity (5000 $W\ mK^{-1}$), strong chemical durability and high electron mobility ($2.5 \times 10^5\ cm^2\ V^{-1}\ s^{-1}$).[12] However, although production of pristine graphene by mechanical exfoliation has led to the rapid development and characterization of graphene's

[a]*Department of Chemical Engineering, University of Waterloo, Ontario, N2L3G1, Canada. E-mail: aipingyu@uwaterloo.ca*

[b]*Chemical Sciences and Materials Systems, General Motors Global Research and Development Center, Warren, 48090, USA*

[c]*National Research Council Canada, 4250 Wesbrook Mall, Vancouver, B.C., Canada, V6T 1W5. E-mail: jiujun.zhang@nrc.gc.ca*

potential, this method is not applicable to most applications which require larger material quantities of graphene. Therefore, some alternative processes are required for large-scale graphene production and its widespread distribution. In recent years, several alternative technologies have been developed graphene production. For example, the patterned growth of graphene by chemical vapor deposition (CVD) on metallic catalysts has proven to have potential in applications requiring the deposition of very thin and highly conductive graphene materials with several layers.[13–16] Direct exfoliation of graphite to graphene can produce low defect ratio materials,[17–25] although limited by large size and thickness distributions, which are useful in bulk applications where graphene is a component within a mixture. In addition, graphene can also be prepared at a larger scale by liquid phase exfoliation to form a graphene oxide (GO) intermediate,[26,27] followed by reduction to restore the graphene structure (rGO).[28–33] However, it has been found that the combination of sheet defects, poor dispersion, restacking and multilayer thickness can prevent the full realization of graphenes' electronic and high surface area properties.[12] In addition, the advanced properties of rGO make it an interesting candidate for many applications.

To overcome the challenges of poor dispersion and restacking, some innovative synthesis methods are definitely necessary in order to achieve long range order and conductivity between the individual graphene sheets.[34] This will be important for maintaining graphene's properties in bulk and to enhance graphene utilization for practical applications. One of the approaches for synthesis of high performing graphene nano-materials is to utilize 2-dimensional graphene sheets to compose solid three-dimensional networks of graphene sponges, which could also be referred to as hierarchal three dimensional structures, foams, templates, and aerogels. These graphene nano-materials, referred to as graphene sponges throughout this review, exhibits high surface area and accessible pore volume as well as high strength and conductivity at extremely low density.

As a result, graphene and carbon nanotube (CNT) based three-dimensional structures are rapidly evolving with many new techniques and applications. They have become the focus of extensive study illustrated by several targeted reviews.[35–39] For those interested in the field, the significant development, wide application scope and numerous variations in preparation methodology continue to make understanding the benefits, future opportunities and drawbacks for these different materials a challenge. This review is intended to address the continued developments and challenges with a wide scope of interest, highlighting fundamental understanding of the synthesis and characterization procedures, future outlook, as

Victor Chabot received his MASc. in Nanoengineering from the University of Waterloo and currently is pursuing his doctoral degree in Chemical Engineering. His research focuses on nanomaterials developments for energy storage and conversion: supercapacitor and battery.

Aiping Yu is an assistant professor at the University of Waterloo in Canada. She obtained her Ph.D. from the University of California-Riverside. Her research interests are in material development for energy storage and conversion, photocatalysts, and nanocomposites. Dr Yu has published over 40 papers in peer-reviewed journals such as Science*, holds multiple patents for graphene nanomaterials and is the author of 2 book chapters and a book on supercapacitors.*

Drew Higgins is a Ph.D. student in Chemical Engineering at the University of Waterloo with an expected graduation date of May, 2015. His research focuses on the development of advanced nanostructured materials for fuel cell and battery applications. He also holds as BASc. ('09) and MASc. ('11), both in Chemical Engineering.

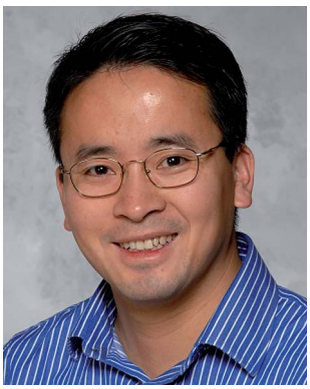

Xingcheng Xiao studied Materials Science and Engineering at the Chinese Academy of Sciences (Ph.D. 2000), and joined the General Motors Global Research and Development Center in 2006. He is currently a staff scientist with focus on surface chemistry and energy storage materials for lithium ion batteries with more than 100 papers publsihed in the peer reviewed journals.

well as an in-depth discussion of application areas reporting high performance in recent publications.

2 Synthesis of graphene and graphene-oxide sponges

Generally speaking, ordered three-dimensional graphene networks can be obtained through different procedures, including the direct gelling of high aspect ratio materials and the self-assembly interactions of GO during reduction. Actually, these techniques share a common drying process for the formation of sponge structure. In the literature, there are several methods including direct drying solution, self assembly and expansion of compact GO films. However, in each method, different reducing species, temperatures and additives can be used according to the targeted products. Bottom-up growth of graphene on metal catalyst supports could offer a fundamentally different procedure for achieving a templated three dimensional architecture on the macroscale, with strictly defined porous sponge structures. Although the procedures in the synthesis methods are slightly different, they share a similar growth philosophy at high temperature, followed by post-treatment to remove the sacrificial support or to grow any composite materials. Table 1 gives a brief summary of the performance metrics associated to the main methods in use to produce free standing graphene architectures. The following subsections will give some deeper discussion on these methods and the research directions of the materials produced.

2.1 Free-standing graphene and graphene oxide sponges

Free-standing graphene and graphene oxide sponges can be produced by a special drying process in which the strong interactions of graphene oxide in water play an important role. In this technique, the interactions are strong enough that solutions could be directly frozen to produce the sponges cost-effectively. Furthermore, the change in hydrophilic character during GO reduction can allow for increased strength and control of pore size, maintaining high area at increased density. However, there are some challenges and the process variability also requires more development for achieving optimal and consistent results.

2.1.1 Direct drying techniques for aerogel preparation. The starting material for generation of graphene and graphene oxide sponges is normally a hydrogel, which can provide a route for the formation of three dimensional graphene structures with extraordinary surface area and properties.[40] The gel commonly consists of a solid network which interacts through physical or chemical bonds to trap many times their weight in water, where hydrophilic groups can create strong surface tension. The surface tension within the gel can prevent the liquid from flowing and disrupting the bonds. To obtain graphene sponge materials by this method, drying the hydrogels is an integral first step for the formation of free standing sponges. However, during drying, the capillary action caused by the evaporation of water can collapse the pore structure. To avoid this, there are two techniques that can be used; one is freeze drying, and the other is critical point drying. Both techniques can be used to limit stress on the pore structure by replacing the liquid with gas for sponge formation. By these techniques, self-assembled structures composed of hydrogel or strong interactions in solution between the 2D sheets can be preserved, resulting in high surface area macroscale sponge. Normally, the freeze drying technique would limit the capillary stress by going around water's triple point boundary, lowering the temperature of water and then going directly from solid to the gas phase *via* low pressure. However, the stress caused by crossing the solid–gas boundary can disrupt more fragile monolayer/bi-layer structures.[41,42] Further, water crystallization on freezing must be

Zhongwei Chen is an Associate Professor in the Department of Chemical Engineering at University of Waterloo. His current research interests are in the development of advanced electrode materials for metal-air batteries, lithium-ion batteries and fuel cells. He received his Ph.D. in Chemical and Environmental Engineering from the University of California-Riverside. Prior to joining the faculty at Waterloo in 2008, he was focusing on the advanced catalysts research in the Los Alamos National Laboratory (LANL) at New Mexico, USA. He has published 4 book chapters and more than 80 peer reviewed journal articles. These publications have earned him to date more than 3000 citations with H-index 28. He is also listed as inventor on 3 US patents and 8 provisional US patents, with two licensed to startup companies in USA.

Jiujun Zhang is a Principle Research Officer and Technical Leader at the National Research Council of Canada's Energy, Mining & Environment Portfolio (NRC-EME). Dr. Zhang is also the Adjunct Professor for 13 universities and research organizations including University of British Columbia, University of Waterloo, and Peking University. Up to now, Dr. Zhang has co-authored 350 publications including 220 refereed journal papers with approximately 10,000 citations, 12 edited /co-authored books, 11 conference proceeding papers, 24 book chapters, as well as 90 conference and invited oral presentations. He also holds over 10 US/EU/WO/JP/CA patents, 9 US patent publications, and produced in excess of eighty industrial technical reports.

Table 1 Summary of graphene/graphene oxide sponge structures and their variants

Synthesis	Characteristics	Application	References
Template growth			
Nickel sponge			
	- Superhydrophobicity (160°, rebounds water) - Flexibility (1 mm bend radius) - Low percolation conductivity (<1 wt%, 5 S cm^{-1})	Polymer composite	118 and 134
	- Up to 130 g g^{-1} organic solvent and oil capacity	Absorber	175
	- High conductivity, 10 S cm^{-1} - High *S*/*N* ratios and sensitivity (2–50× *vs.* glassy carbon) - Direct detection limits below 25 nM	Sensing	115, 120, 147, 149 and 157
	- High rate/capacity retention composite anode materials, up to 200 °C - Free standing electrodes (no binder or metal) - High pseudocapacitance composites, 300–1100 F g^{-1}	Energy storage	121, 122, 227, 230, 231 and 256
Other	- Adjustable macro porosity below 1 μm - Ultralow density reaching 0.2 mg cm^{-3} - High conductivity, 650 S cm^{-1}		124–126 and 128
Free standing			
Direct dry			
	- High strength and rigidity, supports 10 000 g g^{-1} - Conductivity, up to 2 S cm^{-1} - Superhydrophobic, 160° - Scalable size, >1000 cm^3 - Ultralow density graphene network, 0.16–4 mg cm^{-3}	Polymer composite	54–56, 84 and 130
	- Heavy metal ion extraction, 20 mg g^{-1} copper ion - Up to 700 g g^{-1} organic solvent/oil capacity	Absorber	57, 81 and 106
	- 7% DSSC, 2× compared to graphene powder - High initial capacity, reversible capacity of 400 mA h g^{-1}	Energy	53 and 226
Self assembly			
	- Self healing, scratch resistance - Composite with up to 3000% elongation - Conductivity, up to 1 S cm^{-1}	Polymer composite	43, 44, 46, 83 and 87–89
	- High absorption, 600 g $g^{-1}$for organic solvents and 180 mg g^{-1} for dyes - Reversible absorption, can burn off collected contaminants - Rapid compression recovery, up to 90%	Absorber	60, 83, 91, 92, 96 and 174
	- Strong DEFC fuel cell performance and ORR activity better than Pt/C - High rate Li-air battery, 2000 mA h g^{-1} at 2.8 A g^{-1} - High capacity composite anode materials, >700 mA h g^{-1} at 1 A g^{-1} - High capacity/rate composite cathode materials, 400 mA h g^{-1} at 190 °C - High double layer capacitance, 200–480 F g^{-1}	Energy	45, 60, 90, 93, 94, 96, 187, 189, 228, 229, 235, 242, 254 and 255

controlled to prevent sample damage.[43,44] With respect to this, the critical point drying technique has the distinct advantage of avoiding any phase boundary by forming a supercritical fluid at elevated temperature and pressure. However, the critical point of water is at 374 °C, high enough to damage many sponge structures.[40] Instead, acetone is often exchanged for water and then acetone is washed away with liquid CO_2 in a high pressure chamber.[44–46] CO_2 is recognized as an excellent supercritical fluid which exhibits its critical point at only 1000 psi and 31 °C.[40] The pressure in the chamber is slowly released as gas

after the temperature is raised above the critical point, leaving the dry sample with minimal distortion of the gelled structure.

2.1.2 Graphene sponges from the direct drying of graphene oxide hydrogels. Graphene oxide (GO) is currently the most common precursor for the preparation of graphene materials. GO can be prepared by the intercalation and oxidation of graphite powder, usually by the modified Hummer's method, where the key components are sulfuric acid and potassium permanganate.[26,27,31] These two key reactants are mixed to form a strongly oxidizing species known as dimanganeseheptoxide (Mn_2O_7).[47] When heated to around 55 °C and or placed in contact with organic compounds such as graphite, a series of micro detonations occur to functionalize the carbon surface.[47] Therefore, the extent of acid penetration before addition of $KMnO_4$ can greatly affect the exfoliation efficiency. The functionalities consist of primarily epoxide and hydroxyl groups which are highly hydrophilic and form strong hydrogen bonds with water.[48] The intercalation with water can cause lattice expansion, increasing the distance between the graphite planes from 0.335 nm to 0.6–1.2 nm.[49] Then, after strong mixing or weak sonication, the van der Waal's binding forces are easily overcome to form thin mono or few layer graphene oxide materials.[50]

The high solubility and hydrophilic edges of the formed graphene oxide allow it to be well dispersed at high concentrations. However, the basal plane would retain some of its hydrophobicity, rendering GO amphiphilic.[51,52] Then the ungelated solution between 1 and 15 mg mL^{-1}, which exhibits strong enough bonding interactions, can be directly freeze dried to form GO sponges.[53–55] Fig. 1a illustrates the grains created from ice crystal formation during rapid solution freezing, which causes internal expansion and macroscale cracking of the freeze dried solution.[56] Fig. 1b shows images of the well-ordered porous network created by these GO sponges, taken by a scanning electron microscope (SEM).[57] It should be noted that improving the quality and strength of GO networks will be important in the production of repeatable, scalable sponges.

To increase the applicability and harness the desired graphene properties, this GO sponge must be reduced to a rGO sponge. Unfortunately, reintroducing GO sponges to high humidity or water moisture can cause the rapid collapse of the sponge due to the redispersion of GO. This means that the chemical reduction in solution with a reducing agent such as sodium borohydride, hydrazine, ascorbic acid and HI seems unfeasible.[28,30–32,48,58,59] Instead, the GO sponge can be reduced with high temperature (~600–1000 °C) in a dry argon environment or at lower temperatures with a strongly reducing vapor to form rGO sponge.[60,61] Note that in this process, the temperature ramp rate should not be too high, otherwise, the sponge would suffer thermal shock, rapidly releasing gas and disrupting the integrity of the sponge structure.[55] For example, Xue *et al.*[53,62] utilized a porous GO sponge to produce uniformly nitrogen-doped three-dimensional graphene sponge,[53,62] the approach is different from that of the predominantly surface doping seen with reduction of air dried GO powders.[63]

2.1.2.1 Effects of GO sheet size and gelling agents on graphene sponge formation. To produce stronger and more robust graphene sponges from direct drying of GO solutions, understanding the characteristics of GO gelation seems very important. Normally, higher aspect ratio materials are capable of inhibiting rotational motion within a gel and increasing the number of contact points between sheets. Therefore, larger lateral dimensions of the GO sheets should give increased solution viscosity and hydrophobic character. Further, a recent fundamental investigation by Thomas *et al.*[64] determined that up to 33% of the GO produced by oxidation, regardless of the protocol used, is comprised of small over-oxidized carbonaceous debris adhered to the surface of the monolayer GO sheets. A simple wash in base was all that was necessary to effectively remove this debris from the GO surface, revealing its true monolayer nature. Incorporation of a similar step to clean the GO surface during processing could significantly improve the quality of sheet interaction, reduce sheet size distribution and translate to improved performance for the graphene sponges discussed throughout this review.

The investigation by Bai *et al.*[65] into the effect of sheet size and solution acidification revealed that GO hydrogels could also be rapidly formed at room temperature, with a low critical gelation concentration of only 3 mg mL^{-1}. It was observed that the acidification of GO could protonate the carboxyl groups on the basal plane, weakening the repulsive force between sheets and water, making the GO become less stable solution.[65,66] Furthermore, small GO flakes produced through exfoliation of microcrystalline graphite powder or large mesh natural graphite did not form a solid gel, predictably favored the rapid precipitation of flocculated powders after acidification, even at high concentrations. It was also observed that when flake size was greater than 1 μm, instead of precipitating, the restricted rotational motion of the larger sheets and the increased bond strength could trigger a nearly 40× increase in viscosity, forming hydrogels within a few seconds of adding the acid. It should be noted that the initial sheet size is not the only factor,

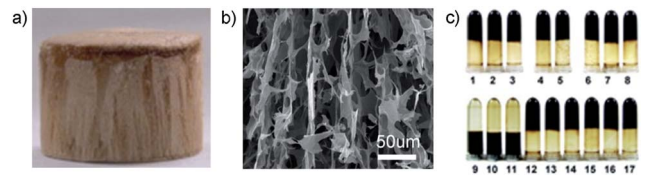

Fig. 1 (a) Image of GO sponge produced by direct freeze drying of GO solution, and (b) SEM of its lateral cross section. (c) Photographs of 5 mg mL^{-1} GO solutions mixed with different cross-linkers: (1) 0.5 mg mL^{-1} PVP, (2) 1 mg mL^{-1} hydroxypropylcellulose (HPC), (3) 1 mg mL^{-1} PEO, (4) 0.1 mg mL^{-1} polydimethyldiallylammonium chloride (PDDA), (5) 0.2 mg mL^{-1} polyethylenimine (PEI), (6) 0.3 mg mL^{-1} cetyltrimethyl ammonium bromide (CTAB), (7) 1.9 mg mL^{-1} tetramethylammonium chloride (TMAC), (8) 0.3 mg mL^{-1} melamine, (9) 20 mM Li^+, (10) 20 mM K^+, (11) 20 mM Ag^+, (12) 15 mM Mg^{2+}, (13) 9 mM Ca^{2+}, (14) 3 mM Cu^{2+}, (15) 3 mM Pb^{2+}, (16) 3 mM Cr^{3+}, (17) 3 mM Fe^{3+}. All the concentrations labeled above are the critical gelation concentration measured for the corresponding cross-linkers, except for 9, 10, and 11 which did not gel. Reproduced with permission from ref. 57 (a and b) and ref. 65 (c). Copyright: 2012 Elsevier (a and b) and 2011 American Chemical Society (c).

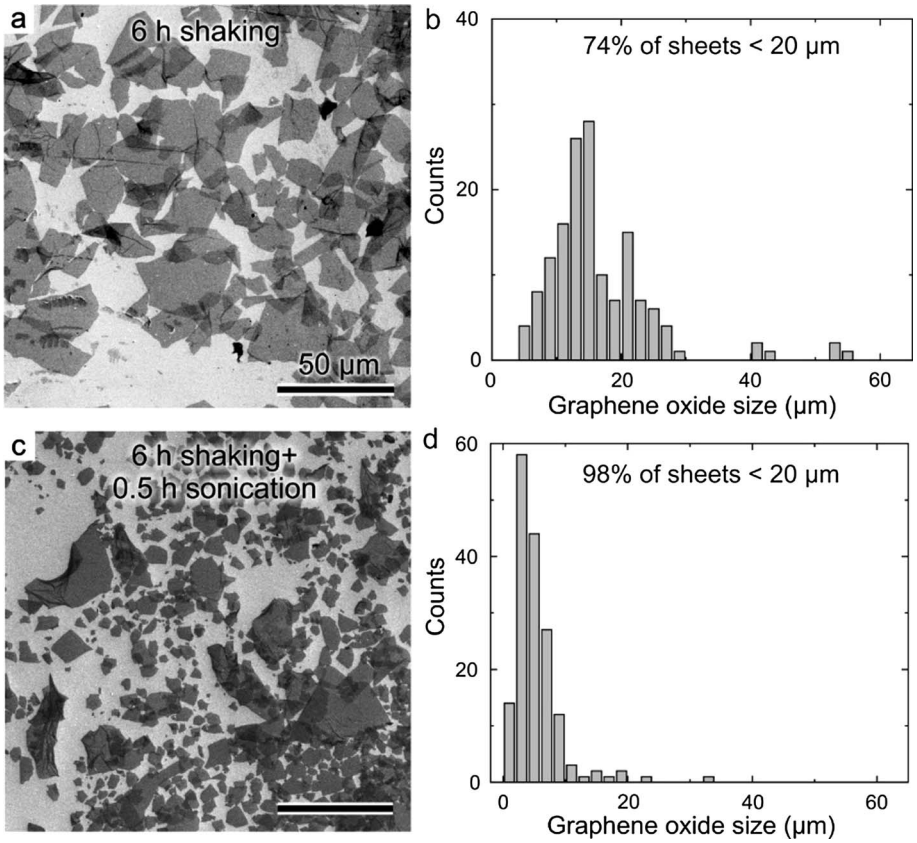

Fig. 2 (a) SEM image of graphene oxide sheets that underwent 6 hours of mechanical shaking. (b) Histogram of sheet sizes observed in (a). (c) SEM image of graphene oxide sheets that underwent 6 hours of mechanical shaking and 0.5 hour of sonication. (d) Histogram of sheet sizes observed in (c). All the scale bars are 50 μm. Reproduced with permission from ref. 67. Copyright 2011 American Chemical Society.

sonication has also be shown to induce scission of the GO basal plane, as observed in Fig. 2.[67–72]

There are also several measures that can be used to strengthen the inter-sheet binding, crosslinking and sharply increase viscosity of the GO solution forming hydrogels which could also translate to the enhanced the properties of the dried aerogels, including: divalent and trivalent coordination with the oxygen functionality on GO,[65,73] long polymer chains which form hydrogen bonds with GO including polyvinyl acetate (PVA), polyethylene oxide (PEO) and polyvinylpyrrolidone (PVP), cationic molecules containing quaternary ammonium groups and protonated amino groups to enhance long range electrostatic interactions (Fig. 1c).[74,75] In addition to these gelating agents, hydrogels have also been prepared by amino acids, nucleosides and peptide chains.[76,77] Depending on the type of stabilizing interactions, some hydrogels will remain intact after washing to form freestanding hydrogels, which can also then be freeze dried to form graphene sponge materials. Chen *et al.*[78] recently demonstrated that this is true for chitosan, a crosslinking polysachharide which can form multiple hydrogen bonds with GO, as well as, amine groups that can strongly attract the negatively charged GO sheets. Hydrogels formed by the addition of polyethylenimine (PEI), crosslinkers at room temperature also exhibit a high density of accessible amine groups, which have been dried to form freestanding graphene sponges with high surface area.[79,80] In contrast to this, the coordination of multivalent ions (La^{3+}, Co^{3+}, Ni^{2+}) to carboxyl groups on the GO sheets offers a selectively reversible sol–gel transition, as observed by Huang *et al.*[80] In this case, the hydrogels could be broken down before drying by the addition of ethylenediaminetetraacetic acid (EDTA), which coordinates with the metal ions in place of the carboxyl groups. With continued investigation into gelling agents, it is expected that the qualities of the GO sponges produced should continue to improve.

With continuing improvements to graphene sponge networks, it is believed that it may be possible to produce the solid material with comparable to or even lower density than air, <1 mg cm^{-3}. For example, the sacrificial template and high temperature CVD approaches discussed later in Section 2.2.3 reveals aerographite could have a density as low as 0.18 mg cm^{-3}. This kind of material benefited from the hierarchical structure, allowing them to reach density much below that of other CNT or graphene sponges reported (>2 mg cm^{-3}). [60] However, the scalability of such materials to large volume using these templating and high temperature processes is limited. Sun *et al.*[81,82] integrated the beneficial effects of giant GO sheets with a 4–50 μm size range. The obtained materials were ultraporous graphene sponges with a density as low as 0.16 mg cm^{-3}. More importantly, the sponges could be achieved with a

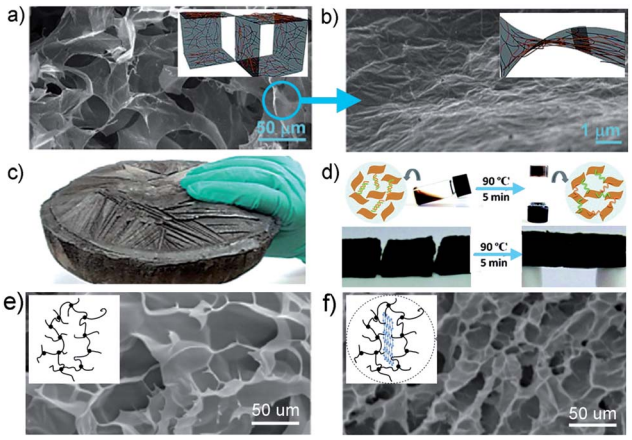

Fig. 3 (a) SEM image and schematic of the CNT/reduced GO sponges (ρ = 1 mg cm^{-33},f_{CNT} = 0.5), and (b) CNT distribution on individual graphene sheets at higher magnification. (c) Demonstration of ~1000 cm^3 sponge cylinder (21 cm in diameter and 3 cm in thickness). (d) Crosslinking (top) and self-healing (bottom) processes of dsDNA/rGO sponge: the as-prepared free-standing sponge was cut with a razor into three small blocks and the blocks could adhere to each other by pushing the freshly formed surfaces to contact together followed by heating at 90 °C in air for 3 minutes. SEM images of freeze dried (e) BIS only sponge and (f) the high elasticity BIS/GO cross-linked sponge. Reproduced with permission from ref. 81 (a–c), ref. 83 (d) and ref. 88 (e and f). Copyright: 2013 Wiley (a–c), 2010 American Chemical Society (d), and 2012 Elsevier (e and f).

simple direct solution freeze drying process, followed by a 90 °C hydrazine vapor reduction[60] which harnessed the leavening effects discussed by Niu *et al.*[61] (Section 2.1.4). However, the formed graphene sponges exhibited a limited mechanical strength and also a limited elasticity due to the flexibility of the large GO sheets. To address this, up to 50 wt% CNTs was added to the GO solution, resulting in a highly synergistic effect through the strong van der Waal forces between the giant rGO and CNTs, which caused the CNTs to lay flat on the graphene sheets (Fig. 3a and b).[60,81] As a result the flexible rGO network favored a load transfer to the strong CNT ribs, creating compressible sponges (0.75–1.5 mg cm^{-3}), which could recover from 50% strain after more than 1000 cycles (88% stress retention). As demonstrated by Fig. 3c, a large 1000 cm^3 brick can be easily made with the rGO-CNT hybrid sponge process.[81] This recent work clearly demonstrates the potential for employing the increased sheet interactions of large graphene sheets to tailor the sponges produced.

2.1.2.2 Direct drying methods with in situ assembled polymer networks. In general, the addition of large chain networks cross linking between the functional groups of multiple GO sheets can help create composites, partially reduced sponges with enhanced strength and elasticity. The improved mechanical properties could also allow the sponges to survive drying more easily. An example was illustrated by Xu *et al.*[83] who considered DNA to be a novel non-covalent crosslinker in the formation of GO sponges. In their work, GO solution was mixed well with double stranded DNA and then heated to 90 °C for 5 minutes, causing the DNA to unwind into its single stranded form. The nucleo-bases and the backbone could form strong pi–pi interactions with the functionalized GO surface, leading GO to rapidly gelate. Upon cooling, the unbound single-stranded DNA (ssDNA) could be converted back to double-stranded DNA (dsDNA) trapped within the final sponge. When cut, the pieces could be touched back together and heated to 90 °C, the unbound dsDNA in the sponge would again unwind and link the partially reduced GO surfaces, giving the sponge a unique self-healing property illustrated by Fig. 3d.

Porous GO sponges have also been reported with the use of polymers to increase their strength and elasticity, as well as prevent dissolution of GO gels. For example, Ye *et al.*[84] reported the usage of low GO concentrations (3–9%) to rapidly crosslink with epoxy monomers, forming porous sponges with high strength and elasticity. After stirring for 1 minute, the mixture was freeze dried to form relatively dense sponges (90 mg cm^{-3}) composed of uncured epoxy monomers and GO. After drying, the sponge was cured at 100 °C for 3 hours. The successful cross linking of the GO sheets was confirmed by the eliminated diffraction peak indicative of both GO and rGO materials. The formed composite epoxy sponge materials could support up to 231 kPa stress at 70% strain. At high stress, the sponges collapsed, similar to other composite sponges.[85–87] Without epoxy, the sponges could still form, but they were weak under deformation and broke under stress, making mechanical tests difficult. Regarding the elasticity, at only 50% strain, the compression showed nearly 100% stress retention after multiple cycles, illustrating a high degree of elasticity due to the presence of crosslinking groups.

Inversely, the crosslinking of GO at low concentration within a polymer matrix can also induce the formation of macroporous polymer sponges with enhanced properties. For example, Shen *et al.*[88] used a free radical polymerization process at 60 °C to generate the GO hydrogels in composite with *N*,*N*-methylenebisacrylamide (BIS) crosslinked polyacrylamide (PAM). In their experiments, no sponge was seen when the BIS crosslinker was eliminated, which was probably due to the lower cross-linking efficiency of GO at 60 °C. However, the introduction of GO to the PAM/BIS gels could increase the number of cross-linked junctions in the polymer microstructure, leading to reduced swelling, enhanced thermal stability and more even distribution of stress throughout the polymer matrix (Fig. 3e and f) (2 mg mL^{-1} GO). The high elasticity of the hydrogel polymers allowed them to recover quickly from compressive stress and reached up to 500% tensile strain before stress failure. Liu *et al.*[89] also reported rubbery composite sponges synthesized using GO to crosslink PAM without BIS initiator. In their synthesis, a longer, low temperature (3 °C) process was used to prevent rapid polymerization and allow more effective GO cross linking (0.6 mg mL^{-1} GO). The resulting hydrogel GO sponges exhibited a long-term stability over 48 hours in water at temperatures up to 80 °C. They also found that PAM hydrogels cross-linked with BIS only were too brittle, breaking easily under compression or stretching, while GO cross-linked hydrogels exhibited up to 4000% elongation before breaking, due to the even force distribution in the pore network and GO's efficient hydrogen bonding with the water network in the sponge.

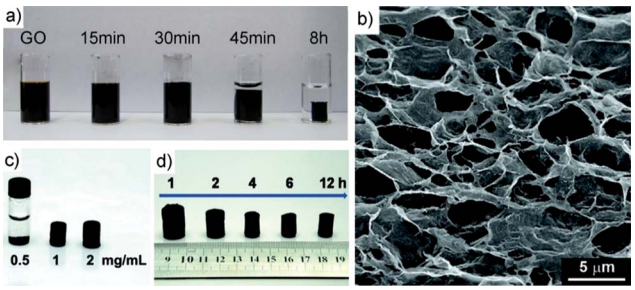

Fig. 4 (a) Photos of GO dispersions after being subjected to ascorbic acid reduction at 100 °C for different periods of time. (b) SEM image of a typical self-assembled 2 mg mL^{-1} rGO sponge formed with 180 °C in autoclave. (c) Image depicts that the GO concentration must be above a critical point before self-assembly will occur and that (d) after a network is formed it will continue to tighten and become denser with reduction. Reproduced with permission from ref. 43 (a) and ref. 90 (b–d). Copyright: 2012 Nature Publishing Group (a) and 2010 American Chemical Society (b–d).

2.1.3 Self-assembled graphene sponges by GO reduction. Three dimensional graphene sponges have also been generated by utilizing the unique properties of graphene oxide to produce high concentration solutions and gels. During the initial stages of thermal reduction, the basal plane of graphene oxide is shifted from a hydrophilic state to a more hydrophobic regime. Hydrogen bonding with water becomes weakened and the van der Waal's attraction between the planes is increased, creating some sticky graphene sheets.[54] If undisturbed, the sheets in solution can began to self-assemble, as illustrated by Qui *et al.*[43] in Fig. 4a. Conversely, Fig. 4c reveals that when the concentration is insufficient, porous precipitates form and settle out of solution.[90] However, if the concentration is high enough, the attractive forces between sheets and the mutual restriction of mobility could result in the slightly reduced graphene materials assembling into a porous hydrogel, taking on the shape of the containment vessel.[91] Reduced further, the C/O ratio of the network was increased, the van der Waal's forces became stronger and the self-assembled rGO hydrogel became more rigid and dense. After, assembly, the structure was dried to prepare sponges. Actually, various approaches for graphene sponges formed by the reduction self-assembly process can be found in the literature in which both high pressure and high temperature in autoclaves, electrochemical reduction or low temperature are used. The reduction can also be performed with the addition of crosslinking agents or more environmentally friendly reducing agents, and the reduction process can be further supplemented with high temperature annealing.

2.1.3.1 Reduction self-assembly by high temperature and pressure. The production of graphene sponge has been widely reported, utilizing an autoclave at moderately high temperatures (~90–200 °C) and elevated solution pressures to reduce GO and induce self-assembly.[43,44,46,90,92,93] Shi *et al.*[90] published several reports on graphene sponges produced from the reduction self-assembly process. In one report, aqueous 2 mg mL^{-1} GO solutions were reduced from the temperature and pressure within an autoclave for 1–12 hours. The process could give some dense hydrogels bound together by many pi–pi interactions and van der Waal's forces.[90] Increasing the reduction time, the C/O ratio was increased from 3.4 (1 hour) to 5.3 (12 hour), and also the conductivity of the unpressed sponges reached to 0.005 S cm^{-1}. Further, as illustrated by Fig. 4d, the sponges become progressively denser as time is increased. The strong rGO sponges were measured to have an elastic regime at low stress and a storage modulus reaching to 470 kPa and stable at measured temperatures up to 100 °C. Fig. 4b shows the thin pore walls of the rGO structure consisting of a few partially overlapping sheets and pore diameter on the order of a few micrometers.

2.1.3.2 Crosslinking enhanced methods for reduction self-assembly. Crosslinkers have also been employed to improve the sheet interactions and or to functionalize the graphene surfaces prepared with high temperature and pressure in an autoclave. For example, Zhao *et al.*[94] produced a 463 $m^2 g^{-1}$ rGO composite by autoclaving a 2 mg mL^{-1} of GO solution in the presence of 5 vol% pyrrole (Py) at 180 °C. In their approach, the nitrogen rich monomer was able to interact with the GO sheets through hydrogen and pi–pi bonding to reduce self-stacking of the GO during reduction, while still promoting binding between rGO. As a result, the sponge volume was 500% greater than that with GO only. Furthermore, the additional sheet interaction allowed the group to achieve three-dimensional sponges with a low critical self-assembly concentration of only 0.5 mg mL^{-1} GO when Py was present. After reduction, the monomer dispersed throughout the hydrogel could be polymerized to strengthen the final freeze dried sponge, lowering the surface area to 166 $m^2 g^{-1}$ but creating a reversible compression. Furthermore, the polypyrrole (PPy) rGO sponge exhibited a high conductivity of 30 S cm^{-1}.[94] Wu *et al.*[93] used various boron and nitrogen to co-dope the graphene planes for the enhancement of electrochemical performance. In this process, a 1.5 mg mL^{-1} GO solution with the co-doping compounds was autoclaved for 12 hours at 180 °C. The resultant sponges exhibited a similar morphology to that previously shown with entangled 1–5 μm pores and thin GO walls of 1–2 nm thickness. Zhao *et al.*[91] harnessed thiourea as a crosslinker additive during autoclaving to produce similar three-dimensional sponges with a maximum compressive stress of 140 kPa. During autoclaving, the thiourea was decomposed to form ammonia and hydrogen sulfide gases which could leaven the hydrogel, creating larger pores. At higher thiourea concentrations, the gas formation could result in looser sponges with poor structural stability. However, at lower thiourea concentrations the gases could dope the basal plane with $-NH_2$ and $-SO_3H$ groups as it was reduced.[91] These groups acted to promote stronger inter-sheet crosslinking, while still increasing the plane spacing compared to rGO. As discussed previously, GO sheet sizes played an important role in forming sponge morphology, having a significant effect on the pore size of the thiourea derived sponges.[91]

It should be noted that the carbon to oxygen (C/O) ratio of the self-assembled rGO sponges reduced through temperature and pressure alone was significantly less than that of graphene powders reduced through hydrazine (C/O ~ 10.3)[28] and $NaBH_4$ (C/O ~ 8.6).[32] But, the rapid gas release during aggressive reduction in these aqueous mediums could limit the

self-assembly behaviour during the reduction of GO solutions prepared by these methods. In the case of self-assembled rGO sponges, the hydrothermally reduced three-dimensional architectures had extensive pore structure that allowed for more efficient gas release than in compact GO films. Therefore, if parameters could be well controlled, most deflagration of the material during reduction at high annealing temperatures could be avoided. Worsley *et al.*[44,46] synthesized partially reduced rGO sponges at only 85 °C from base catalyzed GO solution. Then, the freeze dried sponges were fully reduced by controlled pyrolysis at 1050 °C to produce sponges with low density (6 mg cm^{-3}) and high conductivity reaching to 0.25 S cm^{-1}, comparable to that of the autoclaved rGO sponges. In this approach, before synthesis the GO solutions were sonicated for several hours to ensure uniform mixing. The well-sonicated GO solutions contained smaller GO sheets and the rGO sponges had much smaller pore size compared to those presented in Fig. 3a and 4b. In literature, differences in the GO precursors were likely to create variation in the results achieved between one report and another. However, the low processing temperatures and the steric inter-sheet repulsion created from the unprotonated GO sheets could result in less aggressive restacking/assembly, which after critical point drying produced rGO sponges with 1200 m^2 g^{-1} surface area.[46] The lower temperature could eliminate most of the pressure increase, enabling the reduction process to occur in sealed glass vials. Worsley *et al.*[44] also experimented with the addition of up to 4 wt% loading of resorcinol-formaldehyde (RF) resin to crosslink rGO during resin curing.[44] As a result, conductivity was improved to 0.87 S cm^{-1} but the RF solids could create a stronger restacking of the GO, leading to surface area of only 500 m^2 g^{-1}.

In addition to the controlled high temperature reduction, covalent cross linkers have also been used to demonstrate improved rGO sponge strength and conductivity due to the increased binding strength, flexibility, and control of inter-sheet spacing than with physical interactions alone. Hu *et al.*[92] presented a low density, compression tolerant sponge using ethylenediamine (EDA), a short carbon chain capped with amine groups, to covalently crosslink GO's structure. During 95 °C of reduction, the FTIR band corresponding to epoxy groups on the GO surface weakened, replaced by $-CH_2$ and –NH groups, suggesting that a ring opening reaction occurred on the epoxide groups, leaving EDA covalently bound to the GO surface (Fig. 5a).[92,95] In addition to the mild thermal reduction at 95 °C, EDA was capable of acting as a mild reducing agent, removing hydroxyl functionalities from the GO surface. The EDA could promote covalent linkages between multiple GO sheets, while hydrogen bonds between amine functionalities could further promote inter-sheet binding and the functionalities minimized restacking, thereby eliminating the diffraction peak normally seen for GO and rGO materials (Fig. 5c). The achieved sponge was only mildly reduced (C/O ~ 2.3) and the self-assembly led to very little volume reduction (Fig. 5b). After freeze drying, the functionalized graphene sponges (FGA) were fully reduced by microwave irradiation, which could remove the remaining oxygen and create ultralight sponges (3 mg cm^{-3}) with excellent compressibility at up to 90% strain (Fig. 5d). Luan *et al.*[96] also reported rGO hydrogels which used EDA as a covalent cross-linker, preventing restacking at high concentrations up to 15 mg mL^{-1}.[96] XPS results indicated that nearly all the nitrogen existed in the C–NH–C form, suggesting that EDA was covalently bound to graphene. After EDA linkages were formed at 90 °C,

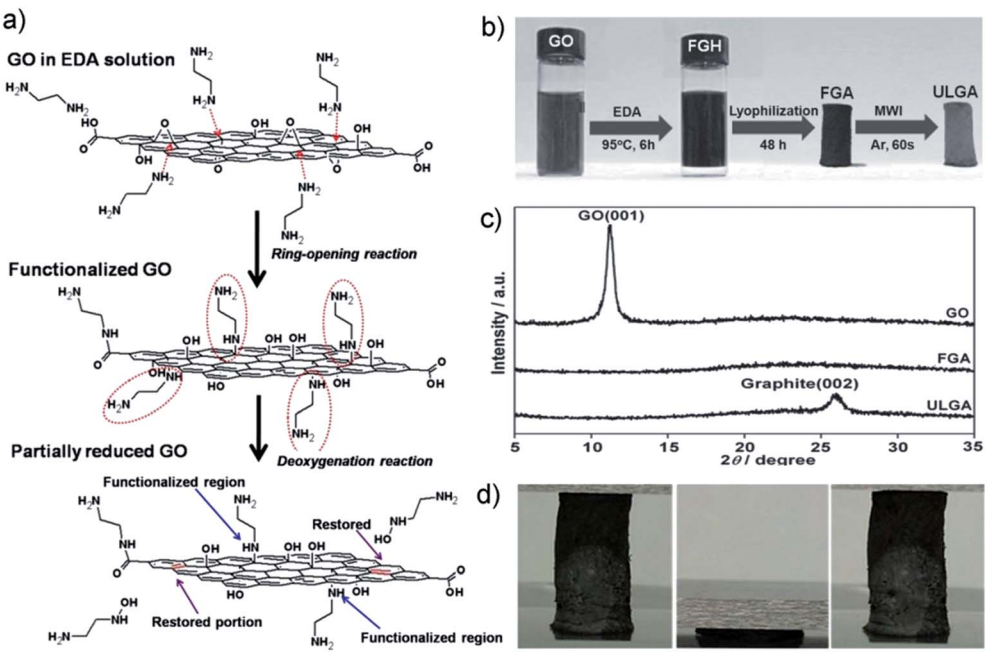

Fig. 5 (a) Schematic illustration of mechanism of EDA-mediated functionalization and reduction of GO, the restored sp^2 regions are marked with red line. (b) Illustration of different steps in the fabrication process of the ultralight graphene sponge (ULGA). (c) XRD patterns and of GO, FGA and ULGA. (d) The digital images showing compressibility of ULGA. Reproduced with permission from ref. 92. Copyright 2013 Wiley.

then the hydrogels were transferred into a hydrazine solution for reduction and finally freeze dried to form a sponge with high surface area of 745 $m^2 g^{-1}$.

2.1.3.3 Low temperature methods for reduction self-assembly. For the synthesis of graphene sponges without high temperature annealing, effective reducing agents are necessary to achieve high conductivity rGO sponges. However, the strong reducing power of the most common agents used, such as hydrazine and $NaBH_4$, could generate large quantities of gas capable of breaking apart the forming hydrogels during their critical state of reduction. Further, the pressure generated during reaction requires the use of high pressure equipment. In addition, hydrazine has high toxicity and $NaBH_4$ has strong reactivity with water. Fortunately, ascorbic acid (AA), also known as "Vitamin C", seems to be an edible, non-toxic mild reducing agent as shown by Fernanadez-Merino *et al.*[30] who demonstrated that AA could be an effective substitute for hydrazine in reducing graphene oxide (C/O $\sim$ 12.5). The proposed reaction mechanism involved a gradual hydride transfer from the AA molecule to the epoxide or hydroxyl groups on GO, releasing primarily water upon heating, as opposed to gases produced by other reduction methods. In addition to ascorbic acid, the mineral salt sodium ascorbate has also been shown as an effective reducing agent for graphene sponge production.[97] Zhang *et al.*[45] illustrated the efficacy of AA by producing comparable rGO aerogels with area of 512 $m^2 g^{-1}$ and conductivity of 0.63 S cm^{-1}, using extended time at only 40 °C in glass vials.[45] In their work, the slow restoration of the pi–pi interaction could result in a strong network and high conductivity, despite the low temperatures used. Qiu *et al.*[43] also reported self-assembled rGO sponges produced by boiling a 5 mg mL^{-1} GO solution containing AA. In addition, they also reported that the gradual reduction allowed for the tuning of the C/O ratio, enabling the production of long range cork-like morphology during freezing. After freezing, the hydrogels were boiled for extended time and freeze dried to form rGO sponges with reversible compressibility. These steps towards more environmentally friendly, low temperature processing with controlled porosity suggest a wide range of application and utility.

Several other low temperature and pressure alternatives have also been successfully demonstrated for graphene sponge formation. As previously discussed above, some crosslinking agents such as EDA and thiourea can also mildly reduce GO and induce reduction self-assembly at moderate solution temperatures around 95 °C, producing robust graphene sponges. In addition to AA, several other reducing agents including $NaHSO_3$, Na_2S, HI, and hydroquinone have been demonstrated to effectively reduce GO and induce sponge self-assembly, using 95 °C and atmospheric pressure.[98] In one embodiment, Chen *et al.*[99] used $NaHSO_3$ to reduce GO and simultaneously trap Fe_3O_4 nanoparticles within the graphene sponge material. By this method they created a superparamagnetic composite with much higher surface area and lower density than for the Fe_3O_4 nanoparticles alone. Another new method demonstrated by Wu *et al.*[100] used copper nanoparticles to simultaneously initiate the reduction self-assembly of GO and generate Cu_2O particles uniformly anchored to the high surface area of the forming graphene sponge. The composite sponges offered excellent photocatalytic degradation of methyl orange and the absorption of several dyes and oils from water. Further, this approach suggests a potentially facile method for formation of high surface area sponges functionalized with metal oxides for a wide range of applications.

An interesting alternative for room temperature processing is the use of electrochemical reduction to prepare rGO sponge coatings with controllable micron size pore structure and low resistance. In this regard, Shi *et al.*[101,102] illustrate low resistance, ultrahigh rate capacitor, electrodes made from interpenetrating networks of electrochemically reduced rGO on gold current collectors. These electrodes displayed relaxation time constants as low as 0.24 ms and strongly capacitive behaviour up to 350 V s^{-1}, faster than even CNT electrodes (time constant, 1.5 ms).

2.1.4 Other techniques for the generation of free-standing graphene sponges. Tightly stacked layers in GO films have also been used to create free-standing graphene sponges. In general, efficient reduction of these GO films seems critical, and can result in varied thickness, due to the shrinking lattice space and the expansion caused by rapid gas formation. For example, in the case of highly efficient reduction by hydrohalic acids, the GO films shrunk in thickness by 50%, while both hydrazine and $NaBH_4$ reduced films broke up or dissolved during the reduction.[48] Another way using thermal shock on GO films could lead to mixed results, achieving well expanded GO films but with loss of film flexibility and embrittlement. To address this, by controlling gas release during the reduction, El-Kady *et al.*[103] exfoliated GO films using a low power laser to slowly leaven and efficiently reduce graphite oxide over multiple cycles. The optimal conditions could produce flexible rGO films (2× thicker than graphite oxide film) with hundred nanometer pores, conductivity reaching to 17 S cm^{-1}, and high surface area of

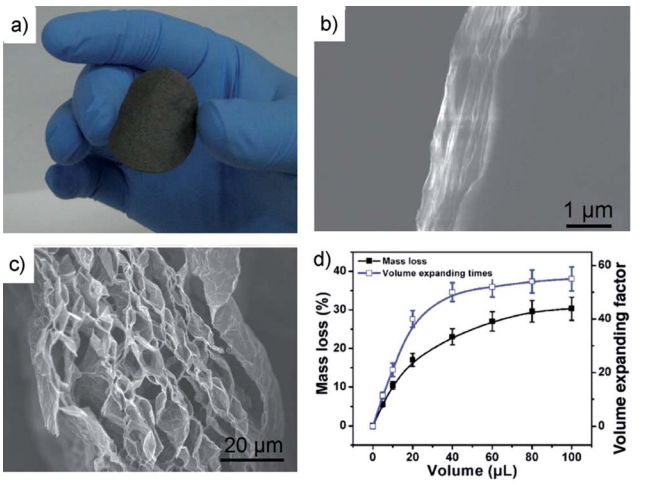

Fig. 6 (a) Freestanding paper-like rGO sponge after leavening a compact GO film in 90 °C hydrazine vapor. SEM images of (b) the rGO formed without any vapor and (c) when 40 μL of hydrazine were added to the autoclave during reduction. (d) A graph depicting the volume expansion with increasing hydrazine vapor content. Reproduced with permission from ref. 61. Copyright 2012 Wiley.

1500 $m^2 g^{-1}$. In a different approach, Niu *et al.*[61] investigated the controlled leavening of tightly packed free-standing graphite oxide films using small quantities of hydrazine to produce flexible three-dimensional rGO papers with surprising mechanical integrity (Fig. 6a). The mass loss through gas generation could result in a significant volume expansion up to 20×, as depicted by Fig. 6b–d.

In addition, when successfully dispersed, high aspect ratio materials such as carbon nanotubes[104,105] and 2D graphene sheets could also develop hydrogels, forming hybrid graphene sponges. As shown in literature,[106] when concentration was increased, the rotational motion of each wire or sheet was inhibited by that of the surrounding molecules, forming a three-dimensional network held together by van der Waal's forces at the contact points. But, there were some challenges in producing this kind of graphene sponges. For example, the reduced graphene oxide and pristine graphene materials might have insufficient functionality due to the structure being dominated by the hydrophobic sp^2 hybridized carbon ring structure; [12,107] and the hydrophobic character could result in poor graphene dispersion, even after continued sonication. Van der Waal's forces between graphene sheets could cause aggregation at low concentration, leading to the material precipitating instead of forming a gel.

Normally, structural preservation of the material upon drying requires the use of solvents compatible with the various drying techniques, often with poor dispersion properties toward graphene or GO. With the addition of surfactant, the quality of graphene dispersion can be greatly improved,[17,23,24,108,109] although this is still not a common technique at this moment. For example, Jung *et al.*[106,109] managed to prepare well dispersed graphene hydrogels by slow volume reduction at 40 °C, which was gelled in a mold and dialysed at 80 °C for a week to remove the surfactant, followed by solvent exchange and critical point drying to collect the sponge. With further development of high concentration dispersion and high temperature treatment to improve the intersheet contacts and remove residual surfactant, graphene sponges with high quality and good properties could be produced from highly dispersed graphene precursor solutions.

2.2 Template guided growth methods

The template growth method, which is a well-defined procedure to grow and effectively separate graphene, can provide a convenient way to control the pattern growth of graphene. Using this method, the resultant graphene materials can have excellent conductivity and reliable long range order. During the synthesis, the sacrificial template, normally a nickel sponge is used as the catalyst layer for graphene growth. This nickel sponge template can provide a robust free-standing application platform or support for material growth. Furthermore, this nickel coating layer can be placed on some predefined substrate shapes to grow graphene/graphene oxide with desired morphologies.

2.2.1 Introduction to growing graphene by chemical vapor deposition (CVD). The chemical vapor deposition (CVD) technique can be used to produce monolayer or few layers of graphene with very high conductivities that are comparable to that of pristine mechanically exfoliated graphene on a small scale.[29] Using this CVD technique, depositing a large area of graphene layers is possible. However, across a large area the graphene layers develop grain boundaries, defects, and multi-layer regions, which may impact the quality of the material. Actually, the production of large area graphene thin films nearly a meter in width using CVD has been demonstrated by a continuous roll-to-roll procedure.[14] In this growth process, three main components are required: a metal catalyst, a carbon precursor and high temperatures around 1000 °C within a controlled atmosphere.

The metal catalyst film is composed of either Ni[110] or Cu[111,112] and is deposited in a thin layer by electron beam evaporation. It is found that the thickness of Ni[13] and Cu[112] layers could affect the surface coverage. For example, using a thinner layer, predominantly mono- and bi-layer graphene could be formed at high temperatures. In some cases, even without any precursor carbon the carbon impurities contained within the deposited Ni films were found to be sufficient for the creation of graphene islands.[113] During the CVD synthesis, carbon can diffuse through the grain boundaries of nickel and migrate toward the interfacial boundaries, when heated at high temperature (900–1000 °C) under argon. The surface segregation can create a thin carbon layer which can then form graphene islands on the metal surface. Similar results can be seen when poly(methyl methacrylate) (PMMA) is used as the carbon source by spin coating, followed by deposition of the metal catalyst thin film.[114] This pathway results in self-limited thickness of graphene films based on metal deposition thickness.[112]

To achieve optimal surface coverage, the predominant method for growing graphene by CVD utilizes the continuous supply of carbon as either vaporized organic liquids such as ethanol[115] and hexane,[116] or small molecule carbon gases such as methane[13,112] and ethane.[117] By this method the carbon solubility in Ni metal is saturated, and upon cooling the carbon solubility decreases and it precipitates on the metal surface, where the carbon atoms organize into a stable graphitic structure. Rapid cooling under argon at 10–100 °C min^{-1} is necessary to limit the formation of multiple layers on the nickel surface.[112,113] Using the CVD technique, the resulting graphene (CVD-G) materials often have a thickness distribution between 1 and 10 layers and their variation is strongly dependent on the synthesis quality.

2.2.2 Growth of graphene sponge from nickel templates. In general, catalysts such as nickel templates (nickel foils) play an important role in deriving large quantities of graphene material. The limited surface area of nickel foils traditionally prevented the extension of CVD-G to a large scale or to a three dimensional structure. To address this, the production of millimeter thick nickel sponges with extremely high porosity (~90–95% void space) and low density (300–600 g m^{-2}) has been made widely available by material suppliers, which has opened new possibilities for CVD-G technology. The rapid development in this area seems to be represented by the work of Cheng *et al.* in 2011.[118] In this work, a Ni sponge was prepared

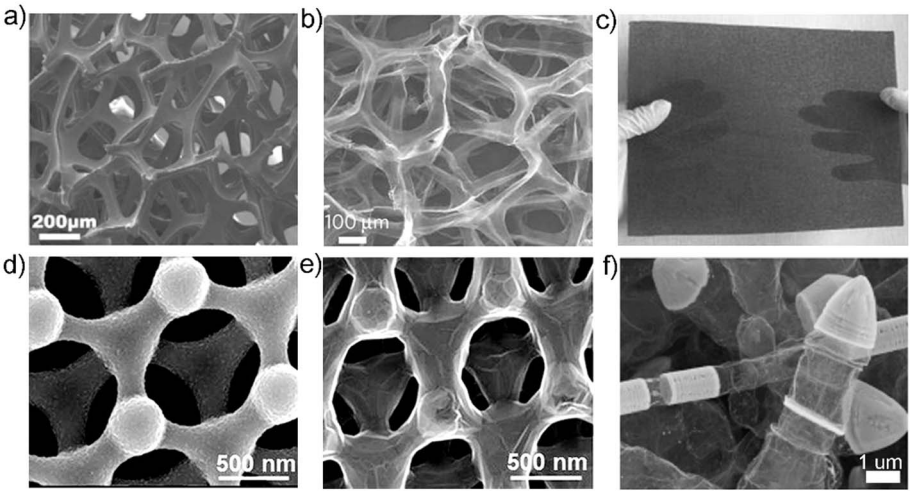

Fig. 7 SEM images of (a) as-grown graphene on Ni sponge surface, (b) CVD-G sponge protected by PMMA after etching the Ni support, (c) the large 374 cm^2 sheets that could be produced by the CVD template method, (d) Ni plated patterned photoresist templates, (e) CVD-G sponge after template removal, and (f) SEM of the graphitic growth during the etching process of the ZnO crystal template. Reproduced with permission from ref. 118 (a–c), ref. 124 (d and e) and ref. 125 (f). Copyright: 2011 Nature Publishing Group (a–c), 2012 American Chemical Society (d and e) and 2012 Wiley (f).

for graphene growth, and the possible surface oxide layer on the Ni sponge was removed by annealing for a short time period at 1000 °C under a 700 standard cubic centimeters per minute (sccm) gas flow composed of 2.5 : 1 Ar : H_2. During synthesis, under a high temperature, a methane carbon source was introduced at a constant rate varying between 2 and 10 sccm. After 5 minutes of carbon gas exposure, a rapid convective cooling step of 100 °C min^{-1} was applied. Fig. 7a shows the resulting graphene coating on the Ni surface with between 2 and 10 layers. The quality of graphene formed was verified using Raman spectroscopy where there was no defect (D-Band) peak for the CVD-G materials. The shape and position of the Raman 2D peak, [119] also suggested a narrow thickness distribution around only a few layers. To obtain the graphene material, following growth of the graphene coating, Ni could be etched away *via* a hot 3 M HCl solution. To avoid collapse of the graphene network a sacrificial PMMA layer could be added before the etching. In doing so, the Ni/G sponge was placed in a 4 wt% solution of PMMA (average molecular weight, 1 million), then a thin layer was formed by baking at 180 °C. After etching away the Ni, the PMMA was gradually removed by placing the CVD-G sponge in hot acetone, which was then evaporated to result in a high surface area graphene monolith (850 m^2 g^{-1}, ~10 S cm^{-1}, as shown in Fig. 7b) with large size dimensions (Fig. 7c). Besides using Ni as the catalyst, monolayer graphene coatings can also be produced using copper sponge, which has a lower carbon saturation level and also exhibits catalytic activity for growth of the graphene materials. The growth produces a similar result, however the growth mechanism for copper differs from that of Ni, and the collapse of the CVD-G sponges could not be prevented when using Cu supports. In addition, Similar high quality CVD-G sponges have been achieved by others using ethanol as the carbon source or with minor variations in flow and temperature.[120–123]

2.2.3 Growth of graphene sponge from other sacrificial templates. Xiao *et al.*[124] reported graphene sponges produced using interference lithography to generate three dimensional patterns of amorphous carbon from a thick layer of NR7 photoresist. The well-defined amorphous carbon structure is covered by a thin layer of sputtered Ni and annealed in N_2/H_2 (Fig. 7d). The sp^3 hybridized amorphous carbon core could diffuse through the nickel layer, forming sp^2 hybridized few layer graphene films. After using acid to etch away the Nickel layer, the templated hollow graphene sponges were produced with defined pores a few hundred nanometers in diameter (Fig. 7e). This process is very similar to that of Ni sponge based graphene sponges but exhibits smaller pore sizes and has the advantage of patterning graphene sponges through existing lithographic processes.

Mecklenburg *et al.*[125] reported ultra-light sponges weighing only 0.2 mg cm^{-3} produced using tunable morphology ZnO networks as a template for CVD growth. The macroscopic ZnO networks were formed by hot pressing loose powders of ZnO with tetrapod morphology to form connective junctions. The ZnO templates were then inserted into a furnace at 760 °C under Ar/H_2 gas flow, and toluene was injected into the furnace slowly. The intake of hydrogen gas could reduce the ZnO forming metallic Zn which could be precipitated out to the exhaust system, but not before the deposition and crystallization of a thin carbon coating. Fig. 7f shows that a thin 15 nm hollow graphitic coating that remains as ZnO is being removed. However, the conductivity of the graphitic sponge was about 0.008–0.37 S cm^{-1} with densities between 0.2 and 100 mg cm^{-3}.

In addition to template growth of graphene, thin films with three-dimensional morphology have also been produced by controlling the drying procedure of the precursor materials creating a self-controlled template. The initial particles

deposited on the surface could act as a guide for the growth of a thick film with porous morphology. These materials vary from the 2D compact reduced graphene oxide (rGO) and graphene oxide (GO) films formed by vacuum controlled restacking, instead they are more similar to the hierarchal structure of the rGO sponges discussed in Section 2.1. The materials exhibit a porous thin film structure that is tunable and the pore walls are composed of few layer graphene. Lee *et al.*[126] fabricated these films of rGO using "breath-figure" templating, which is a well-known technique for synthesizing porous polymer films.[127] In this synthesis, 2.5–5 mL of styrene monomer was mixed with a 3–10 mg mL^{-1} solution of GO sheets. This step could give some polymer-grafted GO sheets (ps-GO) through polymerization, which were uniformly dispersed in benzene. After that, evaporation of the organic solvent under a stream of humid air could induce the self-assembly of the ordered three-dimensional GO film (~1 μm) on a SiO_2 wafer. Thermal treatment was applied at 400 °C in air to remove the polystyrene, followed by 1000 °C under hydrogen to reduce and form the final rGO structure (Fig. 8a).[126] Upon transferring the rGO structure to a polyethylene terephthalate (PET) substrate the thin film proved to be flexible and super hydrophobic, exhibiting a water contact angle of 152°. To improve the material's conductivity, an additional nitrogen doping step was included during pyrolysis to generate a high conductivity of 649 S cm^{-1}. Using a simple low temperature process, Ahn *et al.*[128,129] used a technique known as "nucleate boiling" to induce the self-assembly of solutions containing chemically reduced 2D rGO sheets into ~10 μm thick three-dimensional rGO films (Fig. 8b). Nucleate boiling occurred when a heated substrate was elevated above water saturation point (100 °C). With sufficient heat flux (800–1200 kW m^{-2}), bubbles were formed over the entire heater/substrate plate, grown to a critical size, and then merged into larger bubbles which could compress the rGO flakes between the bubbles. In the final stage of nucleate boiling, the bubbles departed, leaving behind the three-dimensional rGO films with higher conductivity (6.7 S cm^{-1}), comparable to that of CVD-G sponge. Fig. 8c–e shows that the three-dimensional rGO films can deposited on various substrates.

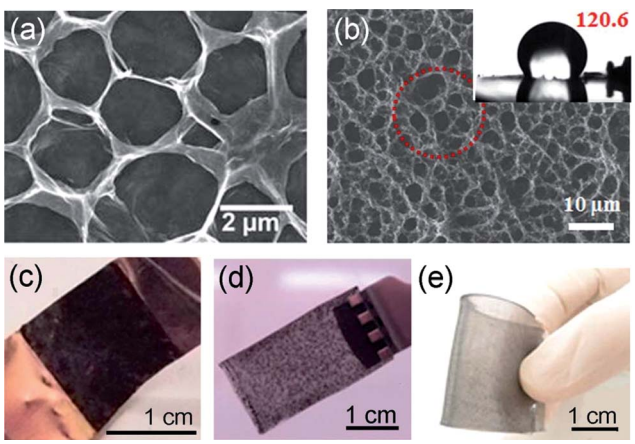

Fig. 8 (a) SEM image of porous film formed from a solution of PS (5 mg mL^{-1})-GO (1.8 mg mL^{-1}), after the removal of the polystyrene content. Pore size and number of layers in the pore wall controlled by PS and GO concentrations. (b) SEM of nucleate boiled structures, inset depicts water contact angle of the film. Depiction of the nucleate boiled coating on the surfaces of (c) FTO glass, (d) Cu foil and (e) PDMS. Reproduced with permission from ref. 126 (a), and ref. 128 (b–e). Copyright: 2010 Wiley (a), and 2013 Nature Publishing Group (b–e).

3 Applications

In the most recent years, graphene-based materials have been developed for many applications, including functional composite materials, electrochemical sensors, absorption agents, and devices for energy storage and conversion.

3.1 Composite materials with tailored functionality

Due to the unique properties of graphene-based materials they can be used as an additive component, forming composite materials with some desired properties and performance. With respect to this, introducing graphene material' properties such as elasticity, porosity, strength and conductivity into the targeted materials are important for many applications. Some graphene sponges are strong under compressive stress, but break under higher loads.[44,46,91,94] As discussed, under certain lower concentration or crosslinked conditions, the formed graphene sponges can exhibit strong reversible compression loads,[43,92] but they still remain fragile during handling. However, the large surface area and high strength of the sponge networks in some optimal mass ratios has made them attractive in providing reinforcement of polymer matrices with increased strength and other tailored properties. Therefore, well-defined graphene sponge matrices can provide high strength, superhydrophobicity and high conductivity, as well as, flexibility or reversible elongation to several compositing applications.

3.1.1 Flexible and conductive polymers. In some applications it is important to promote elasticity and flexibility of the polymer network while preserving high strength and adding conductivity. For example, Chen *et al.*[130] demonstrated this with rigid composite sponges by freeze-drying GO/Functionalized Multi-Wall Carbon Nanotubes (MWCNT) solution which was then pyrolyzed at 1000 °C.[130] The formed low density (40 mg cm^{-3}) sponges could support up to 10 000 times their own weight without collapse, but exhibited an irreversible structural failure at higher loads. In this work, the scaffold was vacuum-infiltrated with polydimethylsiloxane (PDMS) and cured under vacuum at 90 °C, resulting in a flexible composite film, free of aggregation in the reinforcement matrix with a conductivity as high as 2.8 S cm^{-1} using only 1.3 wt% sponge mass. This conductivity was much higher than the 5×10^{-4} S cm^{-1} film created from solution blending PDMS monomer with rGO and the acid-treated MWCNT materials. Further, the robust sponge network within the composited polymer matrix allowed the film to be both bent and stretched (20% tensile strain) many times with negligible drop in conductivity. The strength of graphene sponge scaffolds could also presumably be used to promote strength within stiffer polymer matrices.

The large area sheets of CVD-G sponge with a density of 5 mg cm^{-3} were also produced by Chen *et al.*[118] and used as excellent

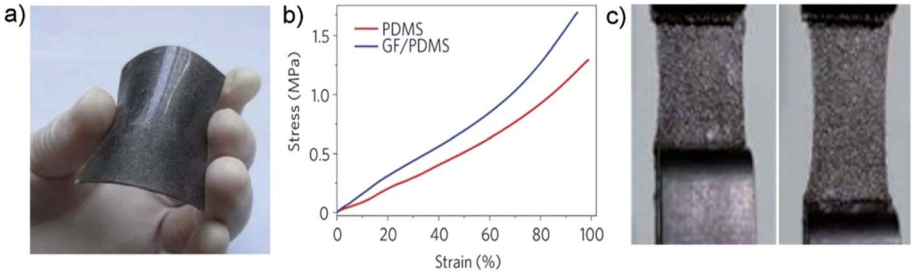

Fig. 9 (a) Photograph of a bent CVD-G sponge/PDMS composite, showing its flexibility. (b) Typical stress–strain curves of PDMS and CVD-G sponge/PDMS composites with ~0.5 wt% of graphene loading and (c) photographs of the stretching process. Reproduced with permission from ref. 118. Copyright 2011 Nature Publishing Group.

scaffolds for infiltration of PDMS. Without PDMS the CVD-G sponge suffered from both poor elasticity and flexibility, limiting its use in flexible electronics. However, the PDMS infiltrated sponge composite in Fig. 9a was able to provide 10 S cm^{-1} conductivity with only 0.5 wt% graphene loading. Secondly, testing showed that the scaffold could increase the tensile modulus of PDMS by 30%, reaching to 95% strain before breaking (Fig. 9b). Further, the conductive networks showed minimal degradation after repeated stretching (50% tensile strain, Fig. 9c) and bending. The strain gauge behaviour after 50% strain showed only a 30% resistance increase compared to the initial state, indicating the adaptability of the reinforced matrix. After 10 000 bending cycles with a small 0.8 mm bend radius, only a 7% increase in resistance was seen.

Unfortunately, infiltration methodologies could sacrifice the inner surface area of the sponge and limit elasticity which is important to some other applications. To address this, an alternative approach is to crosslink polymers with low GO concentration, which can result in porous, polymer reinforced sponges with highly elastomeric behaviour. For example, The composite PAM-GO hydrogels produced by Liu *et al.*,[89] discussed previously, exhibited a 450% increase in tensile strength compared to BIS crosslinked PAM hydrogels, and enabled over 3000% elongation. This was achieved even when the GO content in the hydrogel was only 0.008 wt%. In addition, using only 3 wt % GO, Ye *et al.*[84] produced GO reinforced epoxy sponges with high strength and reversible compression below 70% strain. These sponges still exhibited low density of 90 mg cm^{-3}, similar to that of the soft and brittle GO sponge networks discussed previously.

3.1.2 Superhydrophobic. In general, materials with super hydrophobic surfaces can exhibit self-cleaning, anti-corrosive and anti-fouling behaviours that are desirable properties in the development of many applications. Graphene sheets have a non-polar surface layer, which makes them inherently hydrophobic. Graphene sponges offer a novel approach to creating superhydrophobic surfaces based on a combination of inherent hydrophobicity, tunable Laplace pressure due to controlled pore size, and high elasticity capable of rebounding incoming water droplets. Shin *et al.*[131] illustrate hydrophobicity by epitaxial graphene growth on SiC, which showed a contact angle of 92°, a 30° increase when compared to bare SiC.[131] Like most synthetically prepared hydrophobic surfaces, the hydrophobicity of graphene materials could be enhanced through controlled surface nano/microscale roughness and chemical processes.[132] Due to that the fact that graphene macrostructures have high inherent porosity and surface roughness, near superhydrophobic surfaces (>~150°) could be possible without any coatings. The microscale roughness can result in increased Laplace pressure and if the surface energy was low enough, superhydrophobicity would be reached.[133]

Some superhydrophobic rGO sponges by Lin *et al.*[55] were produced by directly freeze-drying GO, followed by a thermal reduction at 1050 °C (1–5 °C min^{-1} ramp) to form highly hydrophobic surfaces with a 120–130° contact angle. XPS in Fig. 10b reveals that after reduction the C=O and COOH are reduced leaving primarily residual hydroxyl groups (C–O). In this work, superhydrophobicity was reached by utilizing the residual functionality, silanizing the sponges in 30 mL hexane containing 0.1 mL 1*H*,1*H*,2*H*,2*H* perfluorodecyl-trichlorosilane (FDTS) to create a thin conformal coating. The SiCl bonds in FDTS could react with the remaining hydroxyl groups and the remaining fluorine functionality of FDTS could reduce the surface energy of the silanized rGO sponges. The resulting sponges were able to reach a superhydrophobic state, with receding contact angles as high as 160° (Fig. 10c).

Singh *et al.*[134] demonstrated the potential of using low density graphene sponge (CVD-G sponge) to achieve superhydrophobicity, because this material had some well-controlled microscale porosity and roughness with long range order.[134] To make the sponges superhydrophobic, a Teflon solution was drop cast and cured at 165 °C for 24 hours (slightly above the glass transition) to form a smooth conformal coating that was approximately 200 nm thick. Dynamic contact angle measurements on the superhydrophobic Teflon coated sponge showed a significant hysteresis between the receding (144°) and advancing contact angles (163°) as the water droplet shrunk and grew on the surface. The hysteresis was predicted to be from the large 200 μm pore size on the sponges, which caused a pinning of the liquid front during recession, and preventing droplet roll off below 35°. However, the highly ordered pore structure of template CVD-G sponge could help reduce droplets from becoming pinned on impact, a practical issue for superhydrophobic surfaces.[135] On impact, a droplet could be transformed from the predominantly Cassie state, where the droplet rested on trapped air pockets and rolled off the surface, to the

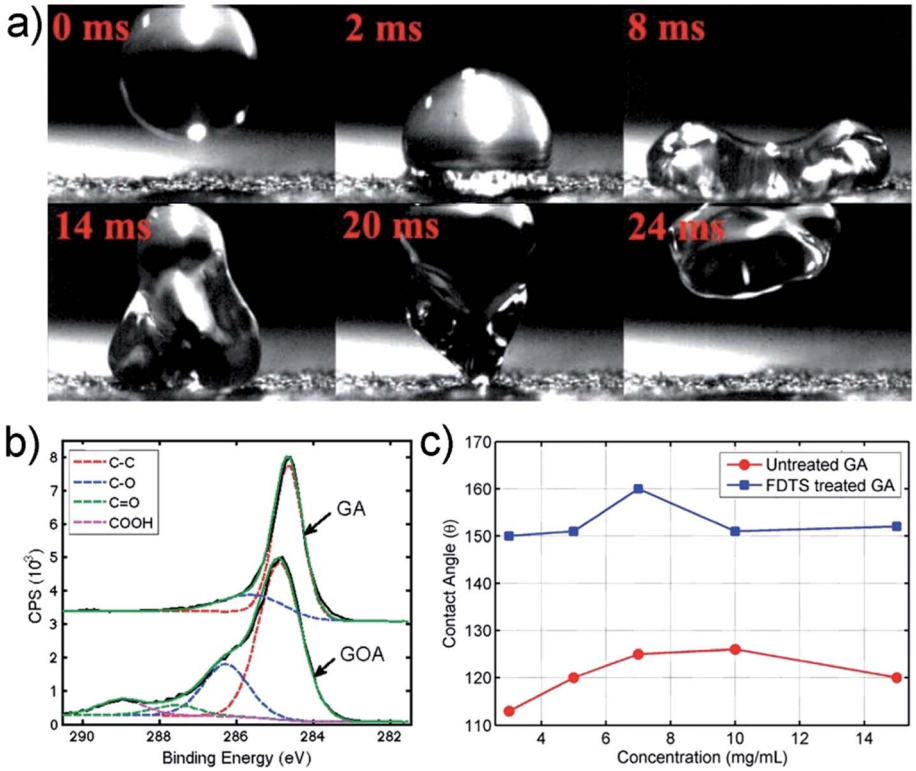

Fig. 10 (a) Snapshots of a water droplet impacting the surface of the Teflon coated graphene sponge. The impact velocity just prior to the droplet striking the surface was ~76 cm s^{-1}. The sequence of snapshots shows the deformation time history of the droplet upon impact. (b) XPS spectra of graphene oxide sponge (GOA) and graphene sponge (GA). (c) Water contact angles of silanized and untreated GA surface with various concentrations. Reproduced with permission from ref. 134 (a) and ref. 55 (b and c). Copyright: 2013 Wiley (a) and 2011 American Chemical Society (b and c).

Wenzel state where the droplet penetrated into the interstices of the roughened surface, becoming pinned on the surface. Using a high speed camera, Singh *et al.*[134] studied the drop impact effect, with large 1.25 mL drops travelling 0.76 m s^{-1} upon impact to see if a Cassie–Wenzel transition could be avoided with the highly ordered CVD-G sponge. When untreated CVD-G sponge was tested, the droplet became completely pinned, and the kinetic energy was quickly dissipated by viscosity during the vibration. When a rigid sacrificial Ni sponge, which had the same pore structure as CVD-G sponge, was coated in Teflon, the transition was avoided as expected, with the drop coming to rest on the superhydrophobic surface after dissipating the vibration energy. Based on the pore size of the Ni lattice, the critical pressure for Cassie to Wenzel state transition was predicted to be 340.2 Pa, well above the 294.3 Pa calculated for the drops impact at 0.76 m s^{-1}. However, Fig. 10a reveals that for the Teflon coated CVD-G sponge, the droplet was able to rebound from the surface at 30% of its impact velocity.[134] The elastic deformation of the graphene sheets within the superhydrophobic G sponge, acted like a spring upon impact, releasing the stored energy back to the droplet and ejecting the unbroken droplet entirely.

3.2 Materials for electrochemical sensors

Graphene sponges that possess excellent conductivity coupled with high surface area have been shown to make an excellent platform for electrochemical sensors to detect trace targets. The large pore systems allow for the rapid analyte transport, resulting in improvement to mediated detection systems which detect a whole range of binding targets such as proteins and enzymes. In direct sensing systems, the graphene itself can detect certain important biological moieties at very low concentrations.

3.2.1 Introduction to using graphene for electrochemical detection. Electrochemical sensors have an advantage over other biosensor transducer methods because they can sense materials without damaging the surrounding system.[136] However, the electro-active groups of the binding proteins and enzymes are generally trapped deep within the protein structure which results in insufficient electron transfer to support sensing.[137,138] For efficient sensing, the distance between the redox centers and electrode surface must be minimized, often by the addition of metal nanoparticles, CNT's or nanowires/fibers. Graphene exhibits excellent electron transfer properties and excellent catalytic activity for detection of several bio-molecule analytes.[137,139] The high conductivity, large surface area and electrochemical activity of graphene have attracted a great amount of interest as a support for high sensitivity enzyme based electrochemical sensing. Further, initial studies also revealed a potential biocompatibility and no obvious toxicity, making rGO based sensors a viable option for *in vivo* biomedical applications.[140–142] Rapid development in this area has led to a long list

of direct electron transfer sensors based on functionalized graphene. Review of these sensors showed they all exhibited long-term stability and high sensitivity detection of important biological moieties including: glucose, Cytochrome-C, NADH coenzyme, Hemoglobin, cholesterol, dopamine and H_2O_2.[137,138] High performance was also seen for non-enzymatic graphene composite sensors which could detect H_2O_2 (ref. 143 and 144) and selectively differentiate dopamine from two common interfering agents such as uric acid and ascorbic acid.[145,146]

Conventionally electrochemical electrodes are limited by the two dimensional nature of electrode surface such as metal and glassy carbon electrodes, which exhibit low active surface area and therefore relatively limited current sensitivity. Graphene sponges with sufficient conductivity and large surface area could be readily applied to similar sensing applications. However, for electrochemical sensing, the abundant defects and functional groups on rGO sponge would limit conductivity and therefore performance, as indicated by Dong *et al.*[147] To improve this, they utilized a highly conductive CVD-G sponge with minimal functional groups, defects and intersheet junctions to demonstrate a variety of three-dimensional graphene sensors with high sensitivity, low noise and low detection limit. Therefore, the monolithic pore network and the high surface area of graphene sponge could be an excellent platform for electrochemical sensing.

3.2.2 Mediated detection. In general, the mediated detection methodology relies on analyte to alter the redox behaviour of a mediator compound in solution to give a stronger electrochemical response of the electrode with improved sensitivity. For example, a phosphate buffered solution containing potassium ferrocyanide ($K_3[Fe(CN)_6]^{3-}$), a commonly employed mediator,[148] was used to compare the performance of CVD-G sponge electrodes with that of conventional glassy carbon. Fig. 11a shows that the peak redox current is over 2× stronger in magnitude for the CVD-G sponge and electrochemical impedance spectroscopy in Fig. 11b reveals the charge transfer resistance and series resistance are significantly smaller for the graphene sponge.[120] Further improvements to mediated CVD-G sponge sensitivity were reported when surface area was increased with the growth of highly conductive CNTs (4× peak increase over GC) or highly electroactive zinc oxide nanorods (25× increase).[115,149] High conductivity of the electrode enabled efficient charge transfer between the highly electroactive ZnO nanorods grown on the graphene surface by precipitation of $ZnCl_2$ at 120 °C.[115] As a result, the ZnO coated CVD-G sponge showed an extrapolated lower detection limit for $[Fe(CN)_6]^{3-}$ of 10 nM (signal/noise, $S/N = 3$), sensitivity of 70 μA M^{-1} cm^{-2} and a linear detection range up to 800 μM.

3.2.3 Direct electron transfer (DET). CVD-G sponge was also investigated for electrochemical sensors based on direct electron transfer (DET) between the analytes and the electrodes. Traditionally DET sensors utilize a fixed enzyme as the sensing region. However, performance is limited by the position and availability of the active sites with the enzymatic proteins, the storage life of enzymes in commercial products, as well as the resistive pathway to the planar electrode surface. In general, three-dimensional electrodes can help enhance the conduction and shorten the distance between active sites. Further the inherent catalytic effects demonstrated by graphene to the redox behaviors of the biological moieties also suggest an improved enzymeless detection schemes if using graphene sponge. For example, DET performance of the effective platform with the assistance of surface bound enzymes was tested using horseradish peroxidise (HRP) for detection of H_2O_2.[149] In this detection, Nafion® was used to fix the HRP and ensure enzymatic activity on the CVD-G platform. The lowest measured detection limit of 1 μM H_2O_2 showed equivalence to the best reported 2D graphene HRP sensors (LOD ~ 1 μM, $S/N = 3$),[138] but with a much higher S/N ratio of 17.4.[137] The superior performance was likely due to the high 138 mA M^{-1} cm^{-2} sensitivity provided by the high surface area three-dimensional sponge.[137] Dopamine detection was used to prove the performance of the three-dimensional platform for enzymeless detection.[115,120,149] Fig. 11c reveals the effect of dopamine concentration on redox current response at 0.16 V measured from cyclic voltammetry of CVD-G sponge in a phosphate buffered solution. It was seen that excellent sensitivity of 620 mA M^{-1} cm^{-2} with linear response up to 25 μM can be achieved. Detection at only 25 nM is easily observed with a S/N of 5.6.[120] Poorer response can be seen for the ZnO coated G electrodes. Furthermore, the addition of CNTs allows a further improved 20 nM detection with a higher S/N ratio of 9.[115,149] It is also seen that the dopamine oxidation response is often heavily confounded by the presence of uric acid (UA) and ascorbic acid (AA) which can be oxidized at nearly the same potential.[138] Fig. 11d illustrates that dopamine's linear response on CVD-G sponge is resolved from the UA peak for measured concentrations as low as 10–20 μM, allowing simultaneous dopamine and UA detection well below the 170 μM simultaneous detection limits seen by Shang *et al.*[146] using 2D graphene sheets.

Dong *et al.*[147] also proved that CVD-G sponge has potential for the enzymeless detection of glucose by additionally growing Co_3O_4 nanowires (Fig. 11e). In their experiments, the wires were grown on a graphene electrode through a 120 °C autoclaved precipitation reaction with $CoCl_2$ and urea, followed by crystallization at 450 °C in a furnace. Two reversible redox transitions occurred between Co_3O_4 ↔ CoOOH(I/II) and CoOOH ↔ CoO_2(III/IV). Charging in the presence of glucose could cause the second transition, at +0.58 V, to exhibit an extraordinary degree of sensitivity (3.39 A M^{-1} cm^{-2}) with a wide range of linear response shown in Fig. 11f (up to 80 μM). The high sensitivity was due to the 850 m^2 g^{-1} surface area and the rapid electrochemical response afforded by the morphology of the cobalt oxide nanostructure and the conductive CVD-G sponge. It was claimed that the response was due to the conversion of glucose to gluconolactone, catalyzed by the conversion of CoO_2 back to CoOOH, which allowed for more electrons to be transferred at the detection sites.[147,150] Remarkably, the limit of detection (LOD) of 25 nM still had an excellent signal to noise ratio of ~8.5 and detection time of only a few seconds.[147] This was far superior to the electrospun Co_3O_4 nanofibers deposited on conventional glassy carbon reported by Ding *et al.*[150] (970 nM, $S/N = 3$), and others for glucose oxidase enzyme fixed to graphene sheets (various reports, LOD ~ 1–1000 μM).[138]

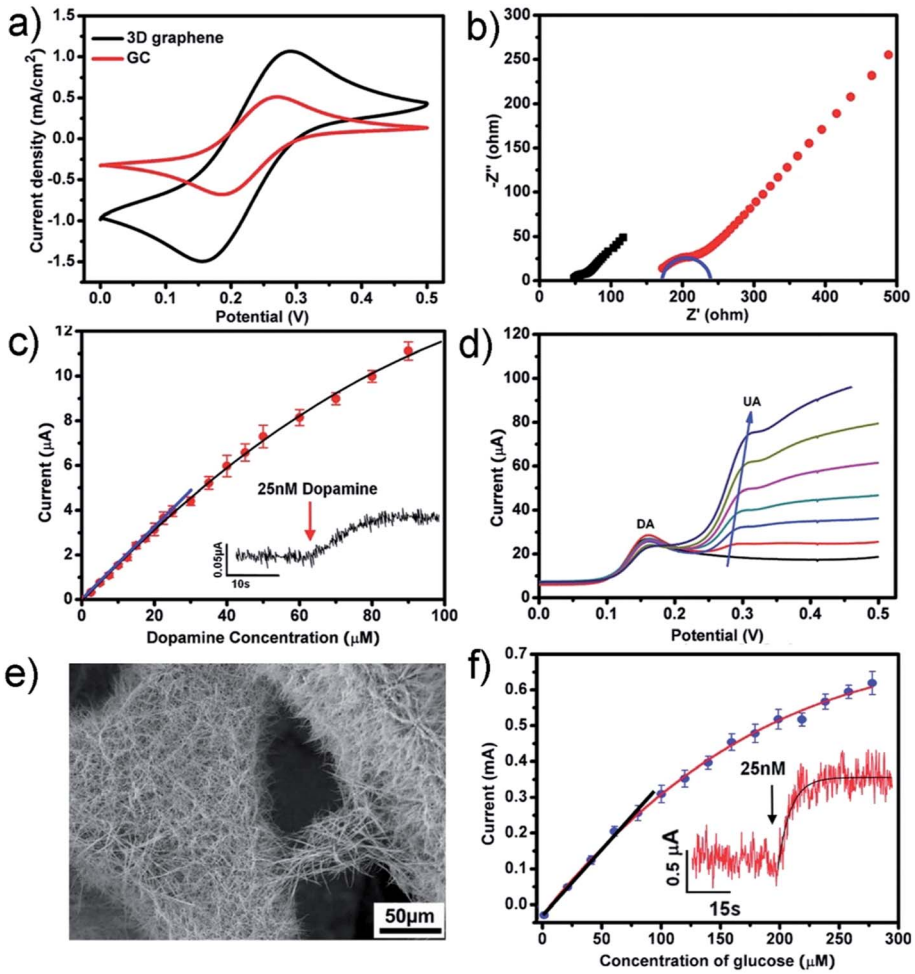

Fig. 11 (a) Cyclic voltammograms and (b) electrochemical impedance spectroscopy (EIS) of glassy carbon (GC) electrode and CVD-G sponge electrode at a scan rate of 20 mV s^{-1} in PBS solution containing 5.0 mM $K_3[Fe(CN)_6]^{3-}$. The charge transfer resistance is fitted on the Nyquist plot as a semicircle; the series resistance is at the *x*-intercept. (c) The average dopamine dose–response curve from CVD-G sponge and the inset shows the amperometric response to 25 nM dopamine. (d) Linear sweep voltammogram (LSV) plots of the graphene sponge electrode in PBS solution containing constant 10 μM DA with different concentrations of UA: 0, 10, 20, 40, 60, 80, 100 μM. Scan rate = 50 mV s^{-1}. (e) High resolution SEM image shows CVD-G sponge coated with Co_3O_4 nanowires for glucose detection and (f) the average glucose dose–response curve when operated in 0.1 M NaOH solution. Reproduced with permission from ref. 120 (a–d) and ref. 147 (e and f). Copyright 2012 American Chemical Society.

3.3 Absorbers

Three dimensional graphene and graphene oxide structures exhibit huge surface area and can be made free-standing, which should provide a large number of active sites for absorption events. Graphene sponges have shown greatly improved uptake of organic liquids compared to existing materials, with the added advantage of reusability. Further, graphene sheets have been shown to absorb certain gases on a molecular level, making for resistive detection of low gas concentrations, and the functional groups on graphene oxide sheets have potential to reduce upon gas exposure to trap and convert undesirable gases in industrial processing.

3.3.1 Gas absorption and detection. The extensive functionality on GO sponges can act as an efficient site for reduction events, leading to physical and resistive detection of gases.[151–153] An example of this phenomena involved the utilization of GO sponges to catalyze the oxidation of SO_2 gas to SO_3 adsorbed on the gas reduced GO sponge at room temperature.[54] After gas exposure, the brown sponges turned black and the trapped SO_3 could be converted to sulphuric acid upon exposure to water, allowing for easy filtration of the rGO impurities. This allowed for visual detection and more importantly the storage of an undesirable industrial gas. Alternatively, high quality graphene sheets exhibit several key properties which make them applicable to ultra-sensitive gas sensing, down to single molecule adsorption events for NO_2.[154] The trace sensitivity of NH_3, HCN, CO, Cl_2 and H_2O has also been shown or modelled by first principle calculations.[155–160] The band structures of single layer sheets can form a zero gap semiconductor with huge surface area. Further, the electronic properties show strong dependence to surface absorbents including gas molecules, and the unique two dimensional crystal lattice can result in low electrical noise and high sensitivity. The change in local carrier density upon

gas adsorption leads to changes in resistance.[154] The restored lattice of rGO graphene sheets was reported to have high gas sensing capability, and when fixed CVD-G sheets were coated with Pd nanoparticles,[160–162] the catalysis of hydrogen gas formed temporary dipole interactions (PdH_x) on the graphene surface, leading to a similar resistance increase upon exposure to less than 100 ppm.[163] In practice, the potential of graphene sheets for sensing is hindered by the susceptibility of individual graphene sheet elements to extraneous environmental and chemical factors, which affect the repeatability and device reliability.

Normally, the use of macroscopic, high surface area graphene sponges with efficient gas transport can enhance the durability and lower the cost targets, while still maintaining high sensitivity for the nanoscale gas interactions. These conductive graphene sponges can exhibit resistive changes upon gas absorption, leading to reversible and highly sensitive detection. For example, Yavari *et al.*[157] reported the use of robust CVD-G sponges to detect toxic NO_2 and NH_3 gases. In their detection, sponge sheets were cut in 0.5 cm^2 strips and fixed to a four probe chip with copper interconnects for creating low contact resistance and reducing electrical noise. The simple and robust sensor design was able to reliably detect resistance change upon exposure to 20 ppm NH_3 and 20 ppm NO_2 gases at room temperature, with steady-state response times around 5–10 minutes. Desorption of the gas was incomplete under pure air, but with joule heating a completely reversible sensor could be achieved. Sensitivity is an order of magnitude higher than that of conducting polymer which was also operated at room temperature and similar time response.[164,165] Thus, the graphene sponge sensors are also more practical for gas detection than semiconducting metal oxide sensors that operate at high temperature (>200 °C).

3.3.2 Organic liquids and dyes absorption. Natural microporous absorbers such as wool, sawdust, expanded perlite and zeolites have been used for spill cleanup. But, these conventional materials have low oil loading and also absorb large quantities of water, making extraction and recycling of the oil absorbents unfeasible.[166–168] Hydrophobic, microporous polymers are mouldable, capable of absorbing 5–25 times their own weight in both oils and organic solvents and up to 80% can be extracted by squeezing.[168–170] As a strong alternative for low-cost oil removal, expanded graphite has shown high loading up to 83 times its weight, and up to 70% of the collected oil can be removed by vacuum filtration. But, the particulates do not exhibit high absorption of organic solvents, the powder form makes for difficult use and the material can only be recycled a few times (only 17% capacity after 5 cycles).[171–173] The development of new materials able to effectively and reversibly remove both organic solvents and oil spill contaminates is critical to the future of oil spill cleanup and water remediation required for environmental protection.

With respect to this, graphene sponges with high surface area, uniform structure, chemical stability in organic solvents, ability to withstand high temperatures, and highly hydrophobic and oleophilic surfaces have been demonstrated to be feasible for absorbers. For example, several graphene and graphene/CNT hybrid sponges have been demonstrated as absorbers for a wide variety of oils, alkanes, water soluble alcohols and organic solvents, with exceptional performance as demonstrated in Table 2.[81,91,175,176] Bi *et al.*[174] used 180 °C autoclaved reduction to induce self-assembly and create an rGO sponge with 430 $m^2\ g^{-1}$ surface area,[174] which showed that this rGO sponge was able to absorb many times its own weight, 20–85 g g^{-1}. Fig. 12a demonstrates a complete absorption of dodecane stained with organic dye from the surface of artificial sea water at an average

Table 2 Absorption capacity of various non-aqueous liquids by graphene sponges

Absorbing species	Adsorption capacity (g g^{-1}) $(M_{after}-M_{before})/M_{before}$	References
Oils		
Gasoline	270	60
Crude oil	289	81
Pump oil	68, 85	174 and 175
Kerosene/paraffin oil	45	174
Castor oil	75	174
Soybean oil	55	174
Diesel oil	124	91
Motor oil	345	81
Olive oil	460	60
Vegetable oil	95, 103, 418	81, 91 and 175
Alkanes		
Hexane	43, 215	81 and 174
Heptane	21, 75	91 and 174
Octane	45	174
Decane	35	174
Dioxane	489	81
Cyclohexane	320	60
Dodecane	50	174
Aromatic compounds		
Ethylbenzene	33	174
1,2-Dichlorobenzene	45, 127, 450	60, 174 and 175
Toluene	55, 125, 200, 350	60, 81, 174 and 175
Nitrobenzene	63, 370	60 and 174
Organic solvents		
Acetic ester/ethyl acetate	92	88
DMSO	62, 430	60 and 145
THF	55, 250	60 and 145
Acetone	51, 350	60 and 145
Chloroform	86, 108, 154, 500, 568	60, 81, 91, 145 and 175
DMF	105	175
Phenoxin	600, 743	60 and 81
Ethylene glycol	133	91
Alcohols and aldehydes		
Methanol	49, 290	60 and 174
Ethanol	51, 80, 300, 350	60, 81, 91 and 174
Ionic liquid		
1-Butyl-3-methylimidazolium tetrafluoroborate	527	81

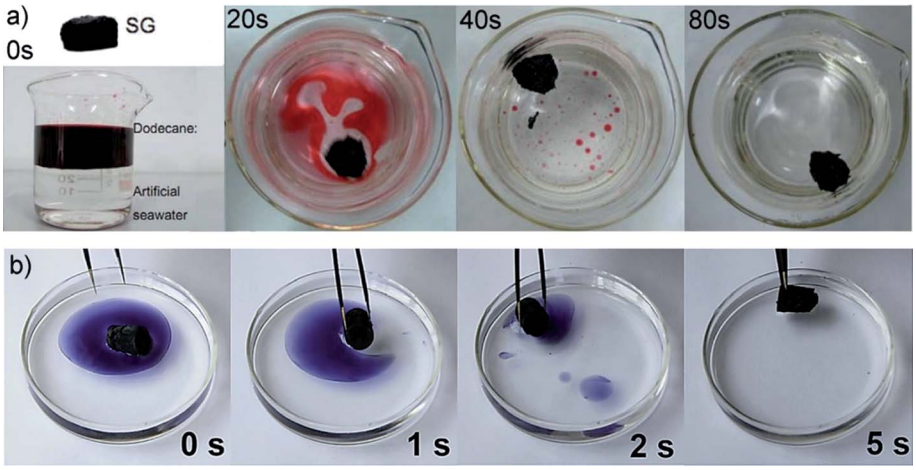

Fig. 12 (a) Photographs illustrating the oil absorption and characterization of a 0.26 g SG block absorbing 11.8 g of dodecane (stained with Sudan red 5B) at intervals of 20 s. (b) Absorption process of toluene (stained with Sudan Black B) on water by the ultra flyweight sponge ($\rho = 1.4$ mg cm^{-3}, $f_{CNT} = 0.5$) within 5 seconds. Reproduced with permission from ref. 174 (a) and ref. 81 (b). Copyright: 2012 Wiley (a) and 2013 Wiley (b).

rate of 0.57 g g^{-1} s^{-1}. Zhao *et al.*[91] reported a 400 m^2 g^{-1} rGO sponge prepared by a similar thermal reduction process but with the addition of thiourea to functionalize and crosslinking the material, and showed that this rGO sponge could even reach even higher adsorption capacities between 75 and 154 g g^{-1}.[91] Moreover dye absorption in water was also test showing high adsorption for common dyes used to color products in industry, such as Rhodamine B (72.5 mg g^{-1}) and Methylene Blue (184 mg g^{-1}). Dong *et al.*[175] utilized CVD-G sponge to achieve 48.5–71 g g^{-1}. It was found that when the macroporous sponges were coated with a dense forest of CNTs, they became super-hydrophobic (152°) due to the increased surface roughness, boosting adsorption capacity to 80–130 g g^{-1}. Even higher dye absorption was observed for the recent graphene/Cu_2O sponges produced by Wu *et al.* reduced using copper nanoparticles.[100] The composite sponges were tested for several dyes including Rhodamine B (150 mg g^{-1}), Methyl Orange (250 mg g^{-1}) and Methylene Blue (650 mg g^{-1}). In addition, a unique property of the metal oxide coated sponge was that it also showed strong photocatalytic degradation properties for Methyl Orange.

Sun *et al.*[81] demonstrated a significantly higher performance and utility of their rGO-CNT sponge prepared by the direct freeze drying of solutions containing giant GO sheets and CNTs.[81] In their experiments, after hydrazine vapour reduction, the GO sheets in the sponge could create a high level of elasticity. Further, the sponge was highly hydrophobic (contact angle, 133°) and had an ultralow density (concentration controlled between 0.16 and 22.4 mg cm^{-3}). More importantly, the method allowed for the scalable preparation of large sponge blocks, an integral feature for the development of materials needed for low-cost, large-scale spill cleanup. The combination of these features allowed the tested ultra-light sponge (1000 cm^3, 1.4 mg cm^{-3}) to reach an absorption capacity of 215–743 g g^{-1}, dependant on liquid density.[81] Fig. 12b shows that the absorption of 1.1 g toluene took only 5 seconds, a rate of 68 g g^{-1} s^{-1}.[174]

Regarding the recyclability of the graphene-based absorbers, due to the thermal stability exhibited by graphene sponges, heat treatment was easily applied to vaporize solvents, allowing the user to reuse the sponge materials (up to 99% capacity remaining after 10 cycles) and restore the absorbed solvent condensate (99.9% restored for future use).[81,174] In the case of compressible sponges, mechanical extrusion could also be used to remove most of the absorbed solvent.[81] The results showed that graphene sponges of various kinds had strong potential to become efficient and safe absorbers for remediation of organic media in environmental protection and industrial processes.

3.4 Energy storage and conversion

Graphene sponges doped or treated with metal oxides, showing limited sheet restacking and high electro-active surface area, have been demonstrated to be excellent materials for devices of energy storage and conversion. Continuing interest for the use of graphene sponges in energy storage is further related to the high conductivity of the interconnected networks, the three-dimensional porous microstructure, high electrochemical stability and the promise of high elasticity and mechanical stability. These devices include the polymer electrolyte membrane (PEM) fuel cells, batteries, solar cells, batteries and supercapacitors. For PEM fuel cells, the graphene materials are normally used the catalysts and catalyst supports; for batteries such as lithium batteries, they are used as both cathode and anode materials; for supercapacitors, they are used as the electrode materials for both double-layer capacitors and pseudocapacitors; and for solar cells, they are used as the dye-sensitizers.

3.4.1 Fuel cells. The most extensively explored fuel cell applications of graphene-based materials are in the area of non-precious metal oxide and nitrogen coordinated metal catalysts, which have been pursued as alternative catalysts to replace expensive platinum catalysts.[176–179] In general, for these kinds of catalysts, both the inferior catalytic activity and stability are insufficient for practical applications when compared to those Pt-based catalysts.[180] Although traditional nanostructured

carbon support materials such as active carbons (carbon black) which have high surface area could greatly improve the catalyst's performance, insufficient chemical/electrochemical stability of these supports are still the limitation. Since graphene-based materials emerged, they have been identified as strong candidates for catalyst applications because of its promising conductivity, high surface area, chemical/electrochemical stability, as well as its strong adhesion to catalyst particles.[176,177,181–184] Furthermore, the abundant functional groups on graphene oxide can provide more chances for the nucleation and anchoring of catalyst nanoparticles, as well as effective molecular and electron transport.[185]

The strong properties of graphene sponge as a catalyst support for platinum was recently described by Wang *et al.*[186] The freestanding CVD G sponges supporting for platinum nanoparticles created improved catalytic performance and durability compared to carbon fiber supports. Recently, Wu *et al.*[187] demonstrated the uniform deposition of iron oxide (Fe_3O_4) nanoparticles onto a graphene sponge framework (Fig. 13a). The sponge was prepared by autoclaving a GO solution containing polypyrrole (PPy) and iron acetate with various concentrations at 180 °C, followed by freeze-drying. The procedure allowed simultaneous self-assembly for Fe_3O_4 particle growth on graphene and incorporation of a nitrogen source into the graphene network. N-doped rGO (3.5 wt% N) sponges containing crystalline Fe_3O_4 nanoparticles were formed by 600 °C thermal treatment under nitrogen gas for 3 hours. Compared to nanoparticles grown on N-doped graphene sheets and carbon black, the N-doped rGO had more positive onset potential (−0.19 V *vs.* Ag/AgCl) for oxygen reduction reaction (ORR) and higher ORR current density (−2.56 mA cm^{-2} @ 400 rpm) in alkaline solutions (Fig. 13b). Further, the electron transfer numbers displayed in Fig. 13c shows that the catalyzed ORR process is dominated by a direct four-electron oxygen reduction mechanism. This is more favorable than that of a two electron transfer process catalyzed by other carbon supports tested.[188] In addition to benefits of increased electrocatalytic ORR activity in alkaline electrolyte, the sponge also revealed better durability than commercial Pt/C (Fig. 13d). Continuing this work, they also reported a similar enhanced performance for ORR in acidic media when Fe nanoparticles were incorporated into the N-doped rGO sponges.[187] Therefore, N-doped graphene sponges should be feasible catalyst support materials for the future non-precious catalysts for PEM fuel cell applications.

The use of rGO sponges has also been recently illustrated by Ren *et al.*[189] by developing rGO supported Ni catalysts for direct ethanol fuel cells (DEFC).[189] High valence nickel oxyhydroxide (NiOOH) as a substitute to platinum has attracted interest because of its high catalytic activity toward ethanol and resistance to poisoning, but its low conductivity and agglomeration require immobilization on a conductive support.[190–196] The composite Ni/rGO sponge was formed by the simultaneous reduction of nickel sulfate and GO at 180 °C in an autoclave.

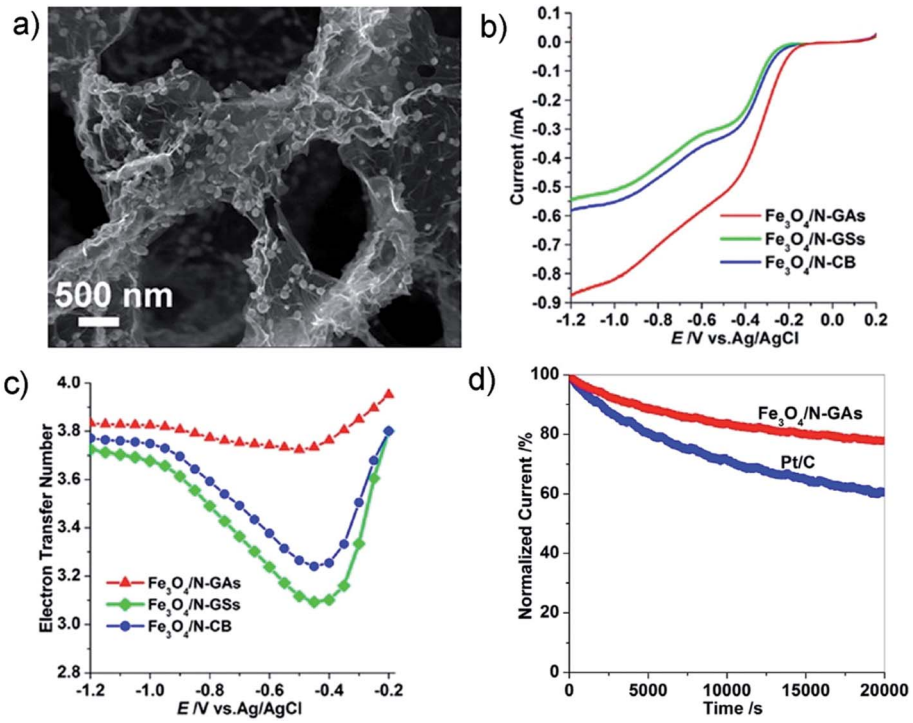

Fig. 13 (a) Typical SEM image of Fe_3O_4/N-GAs revealing the three-dimensional macroporous structure and uniform distribution of Fe_3O_4 nanoparticles in the GAs. (b) RRDE test of the ORR on Fe_3O_4/N-GAs, Fe_3O_4/N-GSs, Fe_3O_4/N-CB in an O_2-saturated 0.1 M KOH electrolyte at a rotation rate of 1600 rpm, (c) electron transfer number of Fe_3O_4/N-GAs, Fe_3O_4/N-GSs, and Fe_3O_4/N-CB as functions of the electrode potential, and (d) the Current-time chronoamperometric response of Fe_3O_4/N-GAs and Pt/C catalysts at −0.4 V. Reproduced with permission from ref. 187. Copyright 2012 American Chemical Society.

The sponge was mixed with diluted Teflon solution to form a slurry and prepared as coating on an ITO glass electrode. Upon electrochemical cycling of this Ni/rGO coated electrode in alkaline media, the nickel nanoparticles underwent a surface oxidation; creating a fast, reversible $Ni(OH)_2$/NiOOH redox transition. When ethanol was added, the redox centers showed a high catalytic activity toward the ethanol oxidation with peak current at a potential of 0.66 V *vs.* Saturated Calomel Electrode (SCE). This DEFC electrode also exhibited a stable catalytic performance, much better than other reported Ni catalysts for DEFC.[190–192] This work demonstrated that graphene sponges could also play a key role in nonprecious catalysis for DEFCs.

Furthermore, graphene-based materials can not only be used as the catalyst supports for both Pt and non-precious metal catalyst, but have also been explored as metal-free catalysts in fuel cell applications, which suggests that graphene sponge materials could also be used in this application. For example, nitrogen-doped graphene materials themselves showed some significant catalytic ORR activity and stability when they are used as the fuel cell catalysts.[197]

3.4.2 Dye sensitized solar cell (DSSC). A typical dye sensitized solar cell (DSSC) has three main components including a dye adsorbed TiO_2 photoanode, a counter electrode and iodide electrolyte.[198,199] In operation, under the light beam on the TiO_2 photoanode, the iodide can be oxidized into triiodide, releasing an electron into TiO_2. This electron will travel through the external circuit to the counter electrode, where it meets triiodide, then reduces triiodide back to iodide. In order to make the trioxide reduction reaction fast enough, a catalyst such as Pt-based catalyst is usually needed.[53] Similar to fuel cells discussed above, a lot of effort has been put on replacing the expensive Pt-based electrodes using non-precious catalysts, specifically with heteroatom doped carbons such as graphene materials although their conductivity and catalytic activities still underperform those of platinum-based catalysts.[200–205] As discussed, graphene sponges could provide a larger surface area for catalytic conversion and well-defined porosity for enhanced electrolyte diffusion. To demonstrate this application, Xue *et al.*[41] used a N-doped rGO sponge (430 $m^2\ g^{-1}$) coated on top of doped tin oxide (FTO) glass as the counter electrode to achieve power conversion efficiency as high as 7.07%, which was comparable to the 7.44% efficiency achieved with a platinum counter electrode and much better than that using undoped rGO sponge (4.84%) or a spin coated nitrogen doped rGO film (4.2%). It was observed that the nitrogen doped rGO sponge could exhibit lower resistance and higher current density than platinum, but a lower fill factor. It was believed that with further optimization, doped graphene sponges could be used as an effective replacement for platinum in DSSCs. Furthermore, some simply prepared nucleate boiled three-dimensional graphene films on FTO glass from Ahn *et al.*[128] were also explored for the counter electrode in quantum dye sensitized solar cells (QDSSCs), and the obtained performance was competitive with the efficiency of more expensive platinum and gold catalysts. The photovoltaic properties of the QDSSCs composed of CdSe/CdS-cosensitized ZnO nanowire anodes and a solid ionomer film electrolyte were tested against various counter electrodes to evaluate the performance of the three-dimensional rGO film structure. The rGO sponge achieved a greater quantum efficiency of 3.6%, compared to only 1.4% for a solution cast two dimensional rGO electrode, 2% for Pt and even 3.4% for Au.

3.4.3 Lithium-ion battery. Graphitic carbon is one of the most commonly used anode materials in commercial lithium-ion batteries. However, to further improve the performance, a new generation of anode materials is necessary to overcome the intercalation capacity limitations of the graphite compounds.[206]

Regarding graphite carbon as the anode material, due to its high crystallinity and packing of the graphene layers, the maximum intercalation state corresponds to LiC_6, where Li transfers its 2s electrons to the carbon host which are stored between two sheets, yielding a limited specific energy capacity of 372 mA h g^{-1}.[207] Second, the long range crystal order of graphite can create large diffusion distances and limit capacity retention at higher rates of charge-discharge. To improve the specific energy capacity, some effort has been made in recent years. For example, Sato *et al.*[208] proposed that disordered carbons could go beyond the ion storage limitation by forming an additional Li_2 covalent site, with each lithium atom trapped on either side of a benzene ring, reaching a maximum theoretical capacity of 1116 mA h g^{-1} in disordered carbon. Alternatively, active defects such as edges and vacancies could be contributing to additional storage of lithium,[209] which was supported by various reports of disordered carbons with some enhancement in capacity (400–700 mA h g^{-1}).[210–212] It seems that the balance among the low conductivity, reduced capacity retention at higher rates and poor cycle life is still the challenge for graphite anode materials.

In this regard, reduced graphene can offer a balance of high conductivity, defects and increased interlayer spacing compared to graphite. The advantages of the two dimensional structure have led to enhanced capacities of 460–800 mA h g^{-1}, varying based on the reduction conditions.[207,213] Unfortunately, although the graphene material could outperform graphite, the rate capability is still low, has poor first cycle efficiency, and even its reversible capacity is still only comparable to the high capacity of nanostructured materials such as tin[214] and metal oxides,[215,216] and much lower than recent advances in silicon based anodes which could achieve a reversible capacity above 3100 mA h g^{-1}.[217] However, these non-carbon materials still suffer from rapid capacity fade during cycling due to pulverization of the electrode, weakening the electrical contact with the current collector. Further, silicon composites with stiff carbon coatings cannot release the large strains created by volume expansion.[218]

As discussed, graphene sheets have a large aspect ratio, are flexible and are highly conductive, suggesting potential as a confining structure to prevent pulverization and improve cycle stability and increase capacity retention at useful discharge rates. It was reported that the performance gains could be realized when agglomeration was prevented by sufficient mixing or anchoring the nanoparticles to the graphene during growth.[219] Zhou *et al.*[218] demonstrated an anode assembly with G/Fe_3O_4, which gave 700 mA h g^{-1} after 100 cycles at 700 mA g^{-1}, two times higher than the reversible capacity of

commercial Fe_3O_4 after 30 cycles at only 35 mA g^{-1}. Xiang *et al.*[220] prepared a layer by layer Si/G composite which retained 800 mA h g^{-1} at 300 mA g^{-1} after 30 cycles, compared to only 400 mA h g^{-1} for silicon particles alone.[220] Evanoff *et al.*[221] used CVD to deposit a uniform coating of Si nanoparticles on graphene powder, enabling a performance of 1400 mA h g^{-1} at a high discharge rate of 1400 A g^{-1}, with negligible performance loss after 150 cycles.[221] The benefits of forming graphene composites were also shown to enhance cathode performance by Hu *et al.*[222] who were able to enhance capacity of commercial $LiFePO_4$ material between 23 and 26% and substantially improve the cycle life by coating the materials with a simple dropwise addition of graphene solution.

Sulfur has a high theoretical capacity of 1672 mA h g^{-1} when it is used as the anode material for batteries, which is many times higher than traditional cathode materials, but similar to many high capacity anode materials, it suffers from low electrical conductivity, dissolution and volume expansion issues which result in poor cycle life. Wang *et al.*[223] showed the use of reduced graphene oxide sheets to wrap the sulfur particles resulting in high specific capacity of 600 mA h g^{-1} at 830 mA g^{-1}, with only 13% decay after 150 cycles. Without the graphene coating, the capacity decreased to less than 330 mA h g^{-1} after only 20 cycles. These results illustrate that two dimensional graphene has a significant potential for the enhancement of both anode and even cathode materials in lithium-ion batteries. The performance results also indicate a future for these materials, reflected by the announcement in early 2013 of two commercial graphene products, XGnP™ and LITX G700™. XGnP™ from XG Sciences is a graphene nanoplatelet material which is being used in a new composite anode to stabilize silicon particles, yielding reversible capacity four times that of current graphite anodes.[224] LITX G700™ from Cabot Corporation have also released a graphene based additive, LITX G700™, which offers enhanced electrical and ionic conductivity in cathode materials at low loading levels that could not be achieved with other carbon additives.[225]

As recognized, increasing porosity of the electrode materials in Li-ion batteries can significantly decrease the diffusion time of lithium ions into the disordered graphene layers, increasing the effective capacity and cycling performance. As a composite, graphene sponges could increase the number of anchoring sites yielding high porosity, resulting in improved capacity. Unfortunately, porosity can reduce the volumetric capacity of the materials and can lead to a large amount of electrolyte intercalation, resulting in increased irreversible capacity like in graphite materials.[206] For example, Zhou *et al.*[226] reported an rGO sponge prepared by thermally annealing a freeze-dried GO sponge. The initial cycle capacity of this material was as high as 1059 mA h g^{-1} (low rate, 50 mA g^{-1}). However, the large surface area of this material resulted in an increased irreversible capacity, indicated by retaining capacity of only 400 mA h g^{-1} (50 mA g^{-1}) after a few cycles and the capacity dropping to 230 mA h g^{-1} (1000 mA g^{-1}) at higher discharge rates. To address this, Xiao *et al.*[227] developed a different procedure (a simple 600 °C CVD process) to grow multilayered graphene sheets vertically aligned on the current collector. As shown in Fig. 14a, the aligned configuration can facilitate both electron and lithium ion transport and increase the active material rate capability, eliminating the need for any conductive additives used in the conventional electrodes. The optimized electrode structure and the reduced diffusion distance, rather than an enhanced diffusion coefficient due to the graphene structure, were believed to be responsible for the fast charge-discharge kinetics seen in Fig. 14b. Therefore, highly ordered porosity must be designed carefully; otherwise it is not a guarantee for the improved battery performance. For these reasons, the benefits of graphene sponge may be more directly applicable to enhancing composite metal oxide and silicon materials.

In the effort to further improve capacity of the electrode materials in Li-ion batteries, Xiao *et al.*[228] studied the performance enhancement of *in situ* Fe_2O_3 growth on GO during autoclaved reduction, resulting in a well anchored composite sponge with a surface area of 77 m^2 g^{-1}, as shown in Fig. 14c. The specific capacity for the sponge was found to be 1000 mA h g^{-1} at 100 mA g^{-1}, and >90% stable for over 50 cycles. This was much higher than the 50^{th} cycle 263 mA h g^{-1} capacity of physically mixed graphene powder and Fe_2O_3 particles. EIS showed that the charge transfer resistance due to ion diffusion was reduced, confirming that the sponge structure could enhance the activity of the Fe_2O_3. Furthermore, the large surface area of the sponge could effectively shorten the diffusion distance, and the anchoring sites formed during rGO reduction could suppress the aggregation and accommodate volume expansion during the cycling. Therefore, over 750 mA h g^{-1} reversible capacity was retained at 1 A g^{-1} (Fig. 14d). Chen *et al.*[229] prepared a similar Fe_3O_4/rGO sponge composite which gave 730 mA h $g^{-1}$of capacity after 50 cycles at a high rate of 1600 mA g^{-1} (~900 mA h g^{-1} at 800 mA g^{-1}), higher than the two dimensional Fe_3O_4 composites previously reported.[208] For validating the materials, the sponges were dispersed in slurries to create the battery electrodes. By breaking up and mixing the sponges, electrodes with a lightweight, conductive, free-standing structure were fabricated for ultralight batteries. An immediate performance advantage could be recognized due to the absence of inactive electrode weight attributed to metal current collectors, conducting additives and binding agents. However, sufficient conductivity is required to support the deposited materials. Ji *et al.*[230] created a CVD-G sponge which showed the sponges ability as an adequate support, by comparing it against both Al and Ni sponge collectors.[230] In all cases, slurries containing carbon black and PVdF were drop cast on the collectors with a loading of 12 mg cm^{-3}. They found that CVD-G sponge actually enhanced columbic efficiency and capacity retention at higher rates, and when considering the mass of the entire electrode not just the active material, the specific capacity of graphene sponge electrodes could outperform aluminum by 23% and Ni sponge by 170%, respectively.

Li *et al.*[231] showed that a conductive CVD-G sponge (10 S cm^{-1}) could be directly used to grow the active anode and cathode materials without inactive mass normally in the slurry, further boosting specific performance of the entire electrode. In this work, the anode was prepared by hydrothermal growth of $Li_4Ti_5O_{12}$ (LTO) on the CVD-G sponge support, as shown in

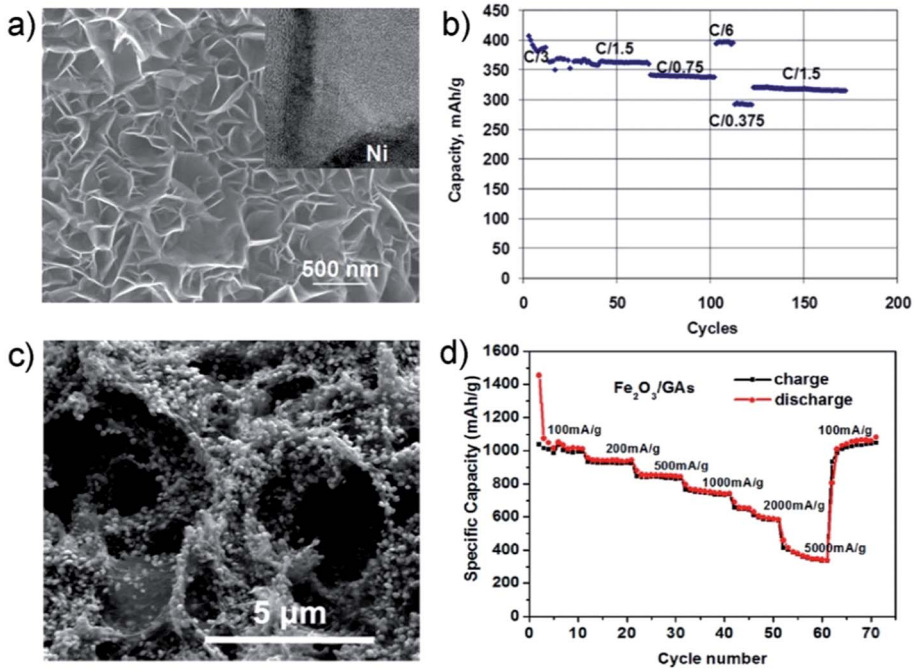

Fig. 14 (a) SEM image of graphene layers grown on Ni substrate. HRTEM (inset) shows graphene layers grown vertically on Ni substrate. (b) Capacity retention of graphene coated Ni-electrode capacity as a function of cycle number. (c) SEM image of Fe_2O_3/graphene sponge (GA) revealing the three-dimensional macroporous structure and uniform distribution of Fe_2O_3 particles. (d) Rate and cycling capacity of Fe_2O_3/GAs tested between 0.01 and 3.0 V. Reproduced with permission from ref. 227 (a and b) and ref. 228 (c and d). Copyright: 2011 Elsevier (a and b) and 2013 American Chemical Society (c and d).

Fig. 15a and b. As tested, the LTO/G anode (Fig. 15c) exhibited a flat potential curve, even at extremely high rates of 200 C (18 second discharge), and the obtained capacity was nearly constant with a power output of 135 mA h g^{-1}. Fig. 15d shows that even after 500 cycles there is only a 4% capacity loss. The LTO/G sponge rate performance was determined to be much better than any previously reported LTO composites, with maximum rates of 10–100 C and much lower capacity retention as well.[232–234] Similar enhancement was also seen for a $LiFePO_4$/G (LFP/G) cathode produced by *in situ* growth of LFP, anchoring it to the CVD-G support. The resulting cathode performance was a reversible capacity of 120 mA h g^{-1} at 10 °C with negligible loss of capacity after 500 cycles.

In general, the lithium diffusion time also plays a significant role in Li-ion battery performance, which can be enhanced with the advent of nanoarchitectures ($t \sim L^2/D$). For example, Yang *et al.*[235] recently reported the one-pot synthesis of a free-standing sponge composed of interconnecting vanadium oxide (VO_2) nanoribbons and rGO sheets, where a mixture of GO and V_2O_5 were reduced inside an autoclave at 180 °C. The composite sponge was dried (SEM in Fig. 16a), pressed and tested as a free standing electrode (specific surface area ~150 m^2 g^{-1}). The tightly interpenetrating VO_2 ribbons were only 10 nm thick, which resulted in a very short diffusion time (~0.01 s). Fig. 16b shows a high reversible specific capacity of 415 mA h g^{-1} at 1 °C and 204 mA h g^{-1} at an extremely high rate of 190 °C (37.2 A g^{-1}, 19 second discharge). Furthermore, the tight network could prevent agglomeration of the VO_2 during cycling which led to stable performance for over 1000 cycles (<10% capacity loss, Fig. 16c). This was significantly improved from bulk VO_2 nanomaterials that showed rapid capacity decay, material distortion and longer diffusion lengths, as well as having limited performance of 130–200 mA h g^{-1} at up to 1 A g^{-1} discharge and a capacity retention of only 20–50% after 50 cycles.[236–239] Therefore, the rGO/VO_2 composite electrode can utilize graphene sponge to greatly enhance the cathode rate capability.

Therefore, it can be seen that the graphene sponges can be used as the both the anode and cathode materials for Li-ion batteries with high discharge rates and the improved performance by significantly reducing inactive electrode mass. Further, combining the CVD-G sponge with higher energy density materials such as metal oxides and silicon can result in much higher volume energy density.

3.4.4 Lithium air battery. Lithium air batteries (Li–O_2) have the potential to store an order of magnitude more energy than current generation lithium-ion batteries. Prototypes consist of a lithium anode, organic electrolyte and a porous carbon cathode exposed to oxygen during operation. However, the largest challenge in Li-air batteries is seen at the cathode side. Upon discharge, the lithium reduces oxygen to form lithium peroxide and/or lithium oxide, which blocks electrolyte and oxygen pathways in the electrode and limit rate capability. This limits the cycle life of the batteries. Further, the tight aggregation of carbon and binder particles results in low O_2 diffusion rates and affects rate performance.[240] Therefore, there is an urgent need for highly effective carbon cathodes with hierarchal porous structure to give higher performance.[241] With respect to this, a

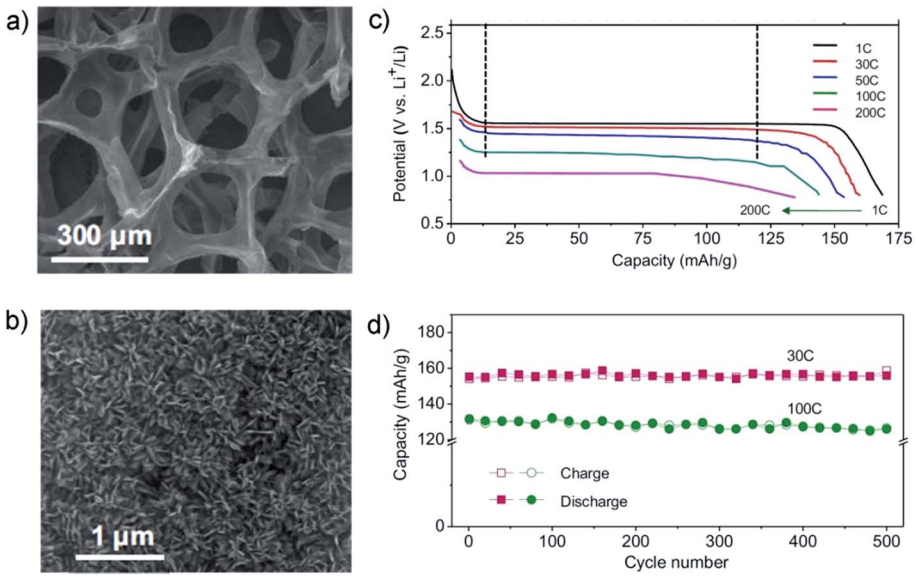

Fig. 15 SEM images of (a) the low resolution G/LTO network and (b) high resolution of the LTO growth on G. (c) Discharging voltage curves of the LTO/CVD-G sponge with different charge/discharge rates. (d) Capacities of the LTO/CVD-G sponge charged/discharged at constant 30 C and 100 C rates for 500 cycles. Reproduced with permission from ref. 231. Copyright 2012 National Academy of Sciences.

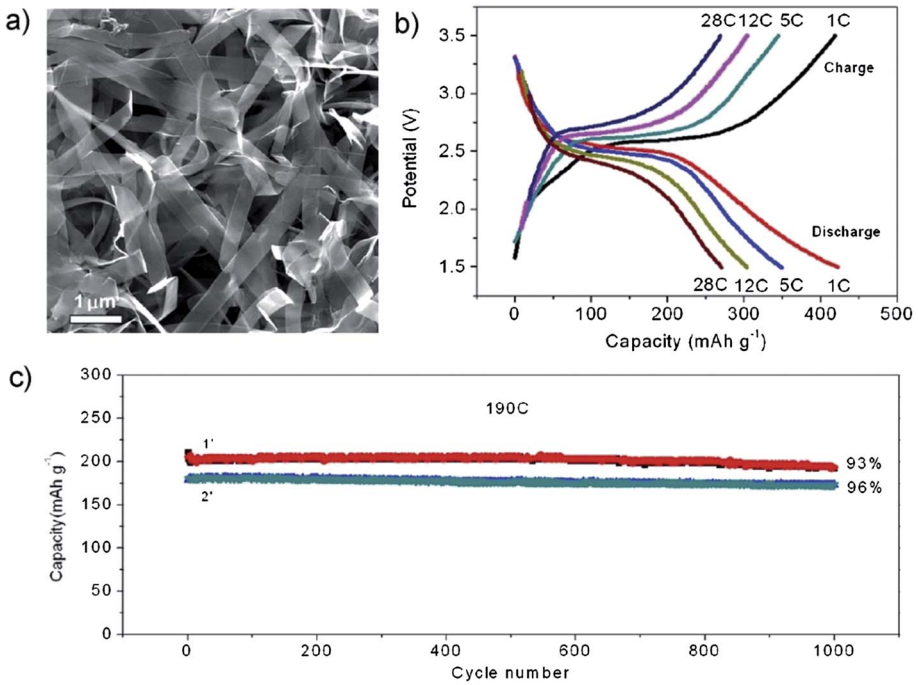

Fig. 16 (a) VO_2–graphene sample hydrothermally treated for 1.5 and 12 h, demonstrating the formation of numerous ribbons with the width of 200–600 nm and length of several tens of micrometers. Electrochemical performance of VO_2–graphene architectures under room temperature. (b) Representative discharge–charge curves of VO_2–graphene (78%) architecture at various C-rates over the potential range of 1.5–3.5 V *vs.* Li^+/Li. (c) Capacity retentions of VO_2–graphene architectures when performing full discharge–charge at the highest rate of 190 C (37.2 A g^{-1}) for 1000 cycles. 1′ and 2′ are denoted as VO_2–graphene architectures with the VO_2 contents of 78% and 68%, respectively. Reproduced with permission from ref. 235. Copyright 2013 American Chemical Society.

high surface area, free standing, open pore system like that of graphene sponges with strong conduction could enhance utilization of porous carbon and allow for efficient transport of electrolyte and oxygen in the cathode. Recently, Wang *et al.*[242] produced a resorcinol-formaldehyde (RF) crosslinked rGO sponge inside the Ni sponge to create a loosely packed, highly conductive cathode composite (specific surface area ~378 m^2 g^{-1}). The micron sized pore structure was able to

better support O_2 transport to the electrode interior, enabling 2020 mA h g^{-1} capacity at a high current density of 2 mA cm^{-2} (2800 mA g^{-1}). Therefore, freestanding graphene supports also have potential to enhance the rate and capacity of next generation Li–O_2 batteries.

3.4.5 Supercapacitor. The chemical stability, large surface area and high conductivity make graphene a natural competitor for the future of electrochemical double-layer capacitors. There are many reports of various graphene and heteroatom doped graphene materials with capacitance between 100 and 200 F g^{-1},[243–250] better than many high surface area activated carbons used in industry.[251] However, restacking of the materials prevents utilization of graphene's full 2600 m^2 g^{-1} surface area, which corresponds to a measured intrinsic capacitance of 550 F g^{-1}, indicating that there is still room for improvement.[248,252] It is believed that assembly of graphene into porous three dimensional supercapacitor electrode layers has the potential to enhance electrode active surface area, boost network conductivity, and create large macropore channels to better facilitate ionic transport in electrolyte. With respect to this, freestanding networks of graphene materials can also reduce inactive electrode mass originating from polymer binders, conductive additives and current collectors.

With optimized processing, the rate performance and capacitance of graphene aerogels can also outperform that of two dimensional graphene. Recently, Mitlin *et al.*[253] illustrated the possibilities for ultrahigh power density graphene-CNT sponge materials in ionic liquids, where ionic liquids traditionally offer very poor rate performance. The electrodes produced with the sponge material exhibited 90–98% capacity retention after 10 000 cycles and stable performance measured up to 100 A g^{-1} or 2 V s^{-1} (~78% of 0.1 A g^{-1} capacitance). The novel single step microwave synthesis was able to generate highly doped and crosslinked sponge-like microscale powders with mesoporous structure. In contrast, the free-standing sponges produced by Shi *et al.*[90] using 180 °C autoclaved reduction of GO without any reducing agents or crosslinkers were able to yield 175 F g^{-1} at 10 mV s^{-1}, 50% better than the standalone graphene particles produced by the same process. However, the freestanding rGO sponge conductivity (0.005 S cm^{-1}) was still not high enough to demonstrate significant performance retention at high rates >50 mV s^{-1} even in aqueous mediums with high ionic conductivity. With continued development, the freestanding rGO sponges underwent secondary processing in 90 °C solution containing a strong reducing agent (HI acid, Hydrazine), the performance was increased considerably due to the enhanced conductivity (0.032 S cm^{-1}).[254] Furthermore, the performance reached to 222 F g^{-1} at low cycle rates and 70% of the capacitance could be maintained at a high rate of 100 A g^{-1} in aqueous electrolyte. Alternatively, freestanding electrodes produced by Wu *et al.*[93] through heteroatom doping during autoclaving gave moderate capacitance at high 100 mV s^{-1} rates, producing between 50 F g^{-1} for the baseline rGO sponge to 132 F g^{-1} for its nitrogen doped counterpart.[93]

In most cases, the high performance demonstrated for graphene sponges is associated to low sponge density due to the relatively low active mass per unit area. In order to produce sponges with smaller pore structure, higher concentrations can be used. However, this may lead to stronger restacking of the rGO, unless some crosslinking functionality is present to prevent restacking. For example, Luan *et al.*[96] used EDA pretreatment to crosslink the rGO sponge before subjecting it to a strong reducing agent, allowing the retention of high surface area >500 m^2 g^{-1} using starting GO concentrations as high as 15 mg mL^{-1}. The tight, porous network could create high conductivity up to 13.5 S cm^{-1} and a performance of 232 F g^{-1} at 1 A g^{-1}.[96,255] Normally, graphene sponges produced by chemical vapor deposition are tightly stacked and uniform due to the low functionality of the as grown structure. As previously discussed, this can lead to much higher conductivity (~10 S cm^{-1}) than most rGO sponges, but also give a low wettability for aqueous electrolytes commonly used in lab scale testing. After mild 80 °C activation in KOH electrolyte to enhance hydrophyllicity, Wang *et al.*[256] demonstrated that the strong supercapacitive performance could also be achieved. CNT-coated CVD-G sponge initially produced only 50 F g^{-1} at 50 mV s^{-1}, similar to the low performance of bare CVD-G sponge, but after treatment the contact angle of the sponge dropped to 19° and the performance was increased to 233 F g^{-1}.[115,147,256] Stability testing on the treated CVD-G/CNT sponge electrode revealed 99% capacitance retention after 80 000 cycles.

Another approach is the *in situ* growth of rGO sponge within nickel foam by a reduction self-assembly process that forms a composite electrode. This methodology provides highly interconnected rGO sheets within the porous sponge with limited restacking and high surface area. Further, the three dimensional nickel foam support creates a short pathway to the highly conductive metal collector and increases the overall strength and durability compared to using free-standing rGO sponge alone. Chen *et al.*[255] illustrated this method by impregnating nickel foam with a 2–6 mg mL^{-1} GO solution, followed by reduction self-assembly at 60–100 °C in ascorbic acid solution. Surface area of the electrode reached 1260 m^2 g^{-1} and the high ion diffusion and electron conduction within the composite electrode enabled outstanding capacitance retention, with capacitance decreasing only 8% for current densities between 1.3 A g^{-1} up to 133.3 A g^{-1}. Shibing *et al.*[257] report a similar binder-free composite electrode composed of *in situ* grown rGO sponge and nickel foam. After annealing the composite electrode, high specific capacitance of 366 F g^{-1} was achieved at 2 A g^{-1}.

Nitrogen doped graphene sponge was also used by Zhao *et al.*[60,94] to report one of the highest capacitive performances of any carbon materials to date. Pyrrole monomer, a carbon ring containing a secondary amine group, was added to an autoclaved GO reduction to form pi–pi and hydrogen bonding with graphene oxide during reduction and freeze-drying. The pyrrole could effectively prevent restacking during reduction and introduce a nitrogen source into the initial sponge structure. The sponges were then annealed at 1050 °C, burning away the pyrrole, leaving a highly conductive (1.2 S cm^{-1}), nitrogen doped graphene sponge (Fig. 17a and b). In this way, nitrogen is believed to be able to modify the electronic structure of pristine graphene, leading to an increased quantum capacitance.[258] As a

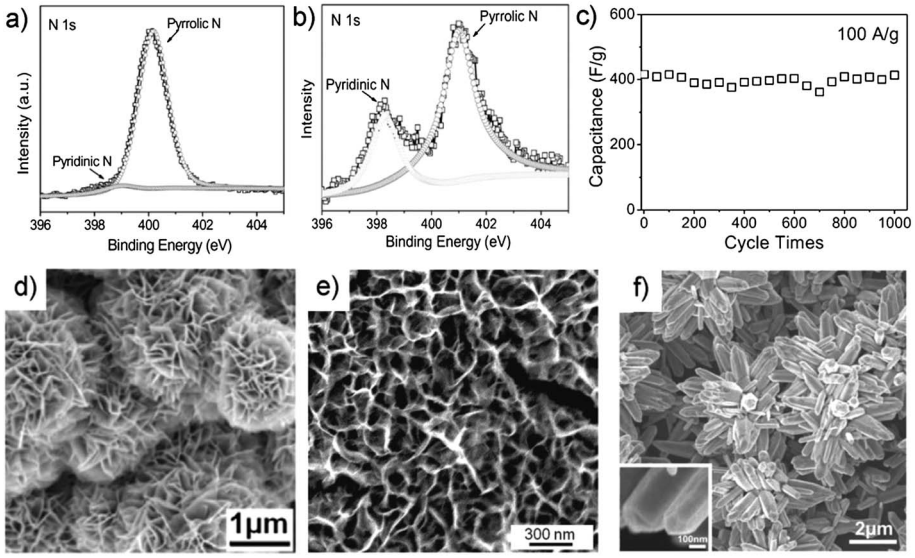

Fig. 17 High resolution XPS spectrum for the N1s peak of the (a) freeze-dried N-containing sponge by hydrothermal treatment of a GO dispersion mixed with 5 vol% Py and (b) the shift to pyrridinic N in the 1050 °C annealed sponge. (c) 1000 cycle stability of the N-doped sponge at a high rate of 100 A g^{-1}. High resolution SEM of well anchored pseudocapacitive CVD-G sponge electrodes coated with (d) MnO_2, (e) NiO and (f) ZnO. Reproduced with permission from ref. 60 (a–c), ref. 121 (d), ref. 122 (e) and ref. 115 (f). Copyright: 2012 Wiley (a–c), 2012 Elsevier (d), 2011 Wiley (e) and 2012 Royal Society of Chemistry (f).

Table 3 Performance characteristics for composites of various metal oxides on CVD-graphene sponge

Metal oxide	Demonstrated morphology	Voltage range (V)	Discharge rate	Capacitance (F g^{-1})	Stability (1000 cycles)	References
ZnO	Nanorods	0.4 V	5–50 mV s^{-1}, 6.7–33 A g^{-1}	210–400	6.7A g^{-1}, negligible losses	115
MnO_2	Nanoflower	1 V	0.2–1.2 A g^{-1}	250–550	0.2 A g^{-1}, 21% loss	121
	Nanoporous particle	1 V	0–100 mV s^{-1}	100–475	~2 A g^{-1}, 8% loss	266
Co_3O_4	Nanowire	0.5 V	10–100 mV s^{-1}, 10–30 A g^{-1}	456–1100	10 A g^{-1}, negligible losses	147
NiO	Nanoporous particle	0.5 V	5–40 mV s^{-1}, 1–20 A g^{-1}	573–816	80 mV s^{-1}, negligible losses	122

result, the performance of the high surface area sponge pressed onto a collector plate could reach to 484 F g^{-1} at 1 A g^{-1}. More importantly, the conductive heteroatom doped structure could retain 400 F g^{-1} at a high discharge rate of 100 A g^{-1} for over 1000 cycles with negligible loss in performance (Fig. 17c).[60] This was even higher than the 350 F g^{-1} (1.5 A g^{-1}) of pseudocapacitive carbon composites created by electro-polymerizing the pyrrole in the rGO sponge in a compression tolerant pseudocapacitive device.[94]

For supercapacitors, using aqueous electrolytes holds several advantages such as high ion mobility, lower toxicity, easy handling, as well as safety compared to organic electrolytes used in commercial electrochemical double layer capacitors (EDLC). However, the low voltage of the aqueous cells limits the energy density. This could be partially overcome by implementing nanostructured metal oxides with fast redox reactions and specific capacitance much higher than double-layer charge storage on carbon.[259–266] Furthermore, metal oxides are more dense, leading to a higher volumetric performance. But, the conductivity of these materials is low, which limits the utilization at the discharge rates required for practical supercapacitive applications. With respect to this, CVD-G sponges could provide some key benefits to enhancing pseudocapacitance. First, the high surface area provides ample area to effectively anchor the growth of nanostructured materials, resulting in short electron transport distances with low transport resistance. In combination, the high conductivity of the graphene network allows for effective utilization of the pseudocapacitive material even at high rates, increasing high power retention and making the cycle life more competitive with EDLC devices. Table 3 lists the composite performance of several nanostructured metal oxides grown on CVD-G sponge materials. Various morphologies of the deposited metal oxides can be seen in Fig. 17d–f and by referring to Fig. 11e. Similar rate enhancement could also be expected for other metal oxides such as RuO_2/2D-G composite powders which have displayed high 570 F g^{-1} capacitance at low 0.1 A g^{-1} rates.[267]

4 Conclusions and outlook for graphene sponge development

4.1 Conclusions

Due to several advantages of both graphene and graphene oxide sponges such as three dimensional graphene networks, high

surface area, high electro/thermo conductivities, high chemical/electrochemical stability, high flexibility and elasticity, extremely high surface hydrophobicity, and so on, they have been used to demonstrate a feasibility way for bridging the nano-scale properties of graphene-based materials to practical macro-scale applications. To facilitate the further improvement and development of these advanced materials, this paper gives a comprehensive review about the most recent progress in synthesis, characterization, fundamental understanding and the performance of graphene and graphene oxide sponges, and their practical applications, including: compositing materials, use as the electrode materials for electrochemical sensors, use as the absorbers for both gases and liquids, and use as electrode materials for devices involved in electrochemical energy storage and conversion. Furthermore, with successful implementation these three dimensional structures offer a larger range of applicability and often greater performance than those achieved with two dimensional graphene.

Regarding the synthesis, several methods have been successfully developed, demonstrating the feasibility in preparing high quality and high performance graphene and graphene oxide sponges. These methods include the templated growth of graphene on nickel sponges, direct sponging of GO solutions, self-assembly and several others. Among these methods, the CVD growth technique can produce well-defined, large pore size structures with high conductivity, and the material's quality can be primarily controlled by process variables during the CVD growth. However, the high temperatures, sacrificial template and multistep processing limit the scalability. The self-assembly technique using the reduction of graphene oxide is compatible with simultaneous growth of composite materials. The properties and performance of the formed graphene/graphene oxide sponges are shown to be strongly dependant on the quality and size of the graphene oxide precursor, the type of the reducing agents, cross linkers, doping agents and the pH of synthetic solution. Although the direct freeze drying self-assembly is simple, it is heavily dependent on size and concentration, in which controlling ice crystal formation and cracking on a larger size scale is a challenge. Therefore, all of the methods reviewed in this paper require further development to promote robust, scalable sponges at low cost and with less restacking. In order to do this, a better understanding of the surface growth and graphene assembly mechanisms is necessary.

Regarding the practical applications, the properties of both graphene and graphene oxide sponges have attracted a great interest, and their feasibilities have also been demonstrated in many practical areas. When they are used to composite the targeting materials such as polymers, the materials' flexibility, elasticity, conductivity, or surface hydrophobicity can be greatly improved; when they are used as the electrode materials for electrochemical sensors, the sensitivity can be significantly increased in trace analysis; when they are used as the absorbers for both gas and liquids extremely high uptake can be achieved; and when they are used as the electrode materials for electrochemical energy storage and conversion devices such as fuel cells, solar cells, lithium batteries, and supercapacitors, significantly improved performance of these devices can be achieved when compared to those using conventional carbon as electrode materials.

4.2 Challenges and future outlook

However, although there are advantages of these graphene-based sponges, to reach large-scale production for commercialization, there are still several common challenges. Most of the sponges discussed throughout this review are on a small lab scale and despite reported flexibility and elasticity, most graphene sponges remain fragile and easily broken or torn without careful handling. This issue must continue to be addressed by future work focused on developing techniques which promote improved inter-sheet binding and composites which effectively incorporate further flexibility and tear resistance. Depending on the application, this might be achieved by the incorporation of highly elastic polymers, surface modification with load bearing fibers or optimization of crosslinking agents that can control structure by selectively targeting either crosslinking of the edge-planes or the basal-plane. With regards to scale, template growth techniques are limited by the furnace size and expense of the sacrificial template, as well as the sheet defects and temperature gradients that exist over larger areas. Future attempts to overcome these challenges might focus on engineering a furnace design capable of accommodating many layers, larger sheets with minimal furnace dead space and promoting uniform graphene growth. Considering the scalability of graphene sponges produced by direct dry and self-assembly methodologies, the freeze-drying process is already available at an industrial scale, but there are many variables which can prevent adhesion of the sponge structure and make it more difficult to reproduce the work reported by others. Additional characterization of the GO precursors, in future work, to determine size and functionality distributions should help mitigate this challenge and could make it easier to predict changes to the binding forces during simultaneous compositing and sponge formation. In addition, the large scale production of GO by current methods is limited by the concentrated acids required and the variability in sheet size, as well as surface functionality. A future direction for graphene sponging technology, might consider controlled surface modification of graphene sheets produced by the solvent or surfactant exfoliation of graphite. In addition to limitations of scale, further development of template supports, direct dry and self-assembly sponges with controlled pore size might be important to commercialization; specifically to enhance volumetric performance for applications such as energy storage and conversion devices, or to optimize the density as an absorber.

Moving forward it is important to recognize simultaneous developments in three-dimensional carbon nanotube sponges that are very similar in function and performance too, but are often prepared by different methods from, graphene sponge. Compared to the often cellular pore structure of graphene sponge, CNT based sponges more strongly favor aligned growth *via* CVD growth or random entanglement *via* functionalized CNTs dried from organo- or hydrogels.[36] However, under

specific growth conditions,[268] it is also possible to produce free-standing non-aligned CVD grown sponges with low density, ultrahigh flexibility and high mechanical durability. Reduced GO sponges have the advantages of higher reported surface area, simultaneous reduction and aqueous sponge formation. But, the high degree of CNT entanglement and high conductivity along their 1D axis may provide more consistency with respect to increased sponge conductivity and mechanical durability during flexibility testing. Looking to the future, the combination of CNT and graphene sponge, may provide enhanced overall performance and mechanical durability.

The key challenges for graphene sponge will require continued innovative research and development. However, in only a short time the extension of graphene from a two-dimensional nano-material into the macro-scale three-dimensional sponges with exceptional performance has been widely demonstrated. Moving forward, utilization of three-dimensional graphene and graphene oxide networks could be integral, harnessing the high-surface area and exceptional properties of graphene materials in order to help achieve the next-generation of performance for several application areas.

Acknowledgements

The authors thank the support of the General Motors Global Research and Development Center. Financial support from the Natural Sciences and Engineering Research Council of Canada (NSERC), and the University of Waterloo are also gratefully acknowledged.

References

1 Y. Zhu, S. Murali, W. Cai, X. Li, J. W. Suk, J. R. Potts and R. S. Ruoff, *Adv. Mater.*, 2010, **22**, 3906–3924.
2 D. Brownson and C. Banks, *Analyst*, 2010, **135**, 2768–2778.
3 B. Thompson and J. M. J. Fréchet, *Angew. Chem., Int. Ed.*, 2008, **47**, 58–77.
4 E. Hammel, X. Tang, M. Trampert, T. Schmitt, K. Mauthner, A. Eder and P. Pötschke, *Carbon*, 2004, **42**, 1153–1158.
5 K. Jong and J. Geus, *Catal. Rev.*, 2000, **42**, 481–510.
6 B. S. Sherigara, W. Kutner and F. D'Souza, *Electroanalysis*, 2003, **15**, 753–772.
7 E. T. Thostenson, Z. Ren and T.-W. Chou, *Compos. Sci. Technol.*, 2001, **61**, 1899–1912.
8 R. H. Baughman, A. a. Zakhidov and W. de Heer, *Science*, 2002, **297**, 787–792.
9 Y. Huang, J. Liang and Y. Chen, *Small*, 2012, **8**, 1805–1834.
10 J. Gooding, *Electrochim. Acta*, 2005, **50**, 3049–3060.
11 K. S. Novoselov, A. K. Geim, S. V. Morozov, D. Jiang, Y. Zhang, S. V. Dubonos, I. V. Grigorieva and A. A. Firsov, *Science*, 2004, **306**, 666–669.
12 K. S. Novoselov, V. I. Fal'ko, L. Colombo, P. R. Gellert, M. G. Schwab and K. Kim, *Nature*, 2012, **490**, 192–200.
13 K. S. Kim, Y. Zhao, H. Jang, S. Y. Lee, J. M. Kim, K. S. Kim, J.-H. Ahn, P. Kim, J.-Y. Choi and B. H. Hong, *Nature*, 2009, **457**, 706–710.
14 S. Bae, H. Kim, Y. Lee, X. Xu, J.-S. Park, Y. Zheng, J. Balakrishnan, T. Lei, H. R. Kim, Y. I. Song, Y.-J. Kim, K. S. Kim, B. Ozyilmaz, J.-H. Ahn, B. H. Hong and S. Iijima, *Nat. Nanotechnol.*, 2010, **5**, 574–578.
15 A. Reina, X. Jia, J. Ho, D. Nezich, H. Son, V. Bulovic, M. S. Dresselhaus and J. Kong, *Nano Lett.*, 2009, **9**, 30–35.
16 G. Eda, G. Fanchini and M. Chhowalla, *Nat. Nanotechnol.*, 2008, **3**, 270–274.
17 A. B. Bourlinos, V. Georgakilas, R. Zboril, T. Steriotis and A. K. Stubos, *Small*, 2009, **5**, 1841–1845.
18 E.-K. Choi, I.-Y. Jeon, S.-Y. Bae, H.-J. Lee, H. S. Shin, L. Dai and J.-B. Baek, *Chem. Commun.*, 2010, **46**, 6320–6322.
19 A. Green and M. C. Hersam, *Nano Lett.*, 2009, **9**, 4031–4036.
20 C. E. Hamilton, J. R. Lomeda, Z. Sun, J. M. Tour and A. R. Barron, *Nano Lett.*, 2009, **9**, 3460–3462.
21 Y. Hernandez, V. Nicolosi, M. Lotya, F. M. Blighe, Z. Sun, S. De, I. T. McGovern, B. Holland, M. Byrne, Y. K. Gun'Ko, J. J. Boland, P. Niraj, G. Duesberg, S. Krishnamurthy, R. Goodhue, J. Hutchison, V. Scardaci, A. C. Ferrari and J. N. Coleman, *Nat. Nanotechnol.*, 2008, **3**, 563–568.
22 U. Khan, A. O'Neill, M. Lotya, S. De and J. N. Coleman, *Small*, 2010, **6**, 864–871.
23 U. Khan, H. Porwal, A. O'Neill, K. Nawaz, P. May and J. N. Coleman, *Langmuir*, 2011, **27**, 9077–9082.
24 M. Lotya, Y. Hernandez, P. J. King, R. J. Smith, V. Nicolosi, L. S. Karlsson, F. M. Blighe, S. De, Z. Wang, I. T. McGovern, G. S. Duesberg and J. N. Coleman, *J. Am. Chem. Soc.*, 2009, **131**, 3611–3620.
25 V. Chabot, B. Kim, B. Sloper, C. Tzoganakis and A. Yu, *Sci. Rep.*, 2013, **3**, 1378.
26 W. Hummers, *J. Am. Chem. Soc.*, 1958, **80**, 1339.
27 D. C. Marcano, D. V. Kosynkin, J. M. Berlin, A. Sinitskii, Z. Sun, A. Slesarev, L. B. Alemany, W. Lu and J. M. Tour, *ACS Nano*, 2010, **4**, 4806–4814.
28 S. Stankovich, D. Dikin, R. D. Piner, K. Kohlhaas, A. Kleinhammes, Y. Jia, Y. Wu, S. T. Nguyen and R. S. Ruoff, *Carbon*, 2007, **45**, 1558–1565.
29 H.-B. Zhang, J.-W. Wang, Q. Yan, W.-G. Zheng, C. Chen and Z.-Z. Yu, *J. Mater. Chem.*, 2011, **21**, 5392–5397.
30 M. Fernandez-Merino, L. Guardia, J. I. Paredes, P. Villar-Rodil, P. Solis-Fernandez, A. Martinez-Alonso and J. M. D. Tascon, *J. Phys. Chem. C*, 2010, **114**, 6426–6432.
31 S. Park and R. S. Ruoff, *Nat. Nanotechnol.*, 2009, **4**, 217–224.
32 H.-J. Shin, K. K. Kim, A. Benayad, S.-M. Yoon, H. K. Park, I.-S. Jung, M. H. Jin, H.-K. Jeong, J. M. Kim, J.-Y. Choi and Y. H. Lee, *Adv. Funct. Mater.*, 2009, **19**, 1987–1992.
33 Y. Qiu, X. Zhang and S. Yang, *Phys. Chem. Chem. Phys.*, 2011, **13**, 12554–12558.
34 Y. Sun, Q. Wu and G. Shi, *Energy Environ. Sci.*, 2011, **4**, 1113–1132.
35 C. Li and G. Shi, *Nanoscale*, 2012, **4**, 5549–5563.
36 S. Nardecchia, D. Carriazo, M. L. Ferrer, M. C. Gutierrez and F. del Monte, *Chem. Soc. Rev.*, 2013, **42**, 794–830.
37 C. Huang, C. Li and G. Shi, *Energy Environ. Sci.*, 2012, **5**, 8848–8868.
38 W. Yeng and G. Shi, *J. Mater. Chem. A*, 2013, **1**, 10078–10091.

39 X. Gui, J. Wei, K. Wang, A. Cao, H. Zhu, Y. Jia, Q. Shu and D. Wu, *Adv. Mater.*, 2010, **22**, 617–621.
40 A. C. Pierre and G. M. Pajonk, *Chem. Rev.*, 2002, **102**, 4243–4265.
41 M. J. Pikal and S. Shah, *Int. J. Pharm.*, 1990, **62**, 165–186.
42 C. J. King and J. Bellows, *Cryobiology*, 1972, **561**, 559–561.
43 L. Qiu, J. Z. Liu, S. L. Y. Chang, Y. Wu and D. Li, *Nat. Commun.*, 2012, **3**, 1241.
44 M. Worsley, P. J. Pauzauskie, T. Y. Olson, J. Biener, J. H. Satcher and T. F. Baumann, *J. Am. Chem. Soc.*, 2010, **132**, 14067–14069.
45 X. Zhang, Z. Sui, B. Xu, S. Yue, Y. Luo, W. Zhan and B. Liu, *J. Mater. Chem.*, 2011, **21**, 6494–6497.
46 M. Worsley, T. Olson and J. Lee, *J. Phys. Chem. Lett.*, 2011, **2**, 921–925.
47 K. R. Koch, *J. Chem. Educ.*, 1982, **59**, 973–974.
48 S. Pei, J. Zhao, J. Du, W. Ren and H.-M. Cheng, *Carbon*, 2010, **48**, 4466–4474.
49 D. R. Dreyer, S. Park, C. W. Bielawski and R. S. Ruoff, *Chem. Soc. Rev.*, 2010, **39**, 228–240.
50 H. He, J. Klinowski, M. Forster and A. Lerf, *Chem. Phys. Lett.*, 1998, **287**, 53–56.
51 J. Kim, L. J. Cote, F. Kim, W. Yuan, K. R. Shull and J. Huang, *J. Am. Chem. Soc.*, 2010, **132**, 8180–8186.
52 P. Guo, H. Song and X. Chen, *J. Mater. Chem.*, 2010, **20**, 4867–4874.
53 Y. Xue, J. Liu, H. Chen, R. Wang, D. Li, J. Qu and L. Dai, *Angew. Chem., Int. Ed.*, 2012, **51**, 12124–12127.
54 Y. Long, C. Zhang, X. Wang, J. Gao, W. Wang and Y. Liu, *J. Mater. Chem.*, 2011, **21**, 13934–13941.
55 Y. Lin, G. J. Ehlert, C. Bukowsky and H. A. Sodano, *ACS Appl. Mater. Interfaces*, 2011, **3**, 2200–2203.
56 X. Zhou and Z. Liu, *Chem. Commun.*, 2010, **46**, 2611–2613.
57 X. Mi, G. Huang, W. Xie, W. Wang, Y. Liu and J. Gao, *Carbon*, 2012, **50**, 4856–4864.
58 J. J. Yoo, K. Balakrishnan, J. Huang, V. Meunier, B. G. Sumpter, A. Srivastava, M. Conway, A. L. M. Reddy, J. Yu, R. Vajtai and P. M. Ajayan, *Nano Lett.*, 2011, **11**, 1423–1427.
59 M. D. Stoller, S. Park, Y. Zhu, J. An and R. S. Ruoff, *Nano Lett.*, 2008, **8**, 3498–3502.
60 Y. Zhao, C. Hu, Y. Hu, H. Cheng, G. Shi and L. Qu, *Angew. Chem.,Int. Ed.*, 2012, **51**, 11371–11375.
61 Z. Niu, J. Chen, H. H. Hng, J. Ma and X. Chen, *Adv. Mater.*, 2012, **24**, 4144–4150.
62 H. Wang, T. Maiyalagan and X. Wang, *ACS Catal.*, 2012, **2**, 781–794.
63 L. Qu, Y. Liu, J.-B. Baek and L. Dai, *ACS Nano*, 2010, **4**, 1321–1326.
64 H. Thomas, S. Day, W. Woodruff, C. Vallés, R. Young, I. Kinloch, G. Morley, J. Hanna, N. Wilson and J. Rourke, *Chem. Mater.*, 2013, **25**, 3580–3588.
65 H. Bai, C. Li, X. Wang and G. Shi, *J. Phys. Chem. C*, 2011, **115**, 5545–5551.
66 H. Bai, C. Li, X. Wang and G. Shi, *Chem. Commun.*, 2010, **46**, 2376–2378.
67 S. Pan and I. A. Aksay, *ACS Nano*, 2011, **5**, 4073–4083.
68 M. McAllister, J. Li, D. Adamson, H. Schniepp, A. Abdala, J. Liu, M. Herrera-Alonso, D. Milius, R. Car and R. Prud'homme, *Chem. Mater.*, 2007, **19**, 4396–4404.
69 J. Zhao, S. Pei, W. Ren, L. Gao and H. Cheng, *ACS Nano*, 2010, **4**, 5245–5252.
70 L. Zhang, J. Liang, Y. Huang, Y. Ma, Y. Wang and Y. Chen, *Carbon*, 2009, **47**, 3365–3368.
71 C. Botas, A. Pérez-Mas, P. Álvarez, R. Santamaría, M. Granda, C. Blanco and R. Menéndez, *Carbon*, 2013, **63**, 576–578.
72 G. Qi, J. Cao, R. Bao, Z. Liu, W. Yang, B. Xie and M. Yang, *J. Mater. Chem. A*, 2013, **1**, 3163–3170.
73 S. Park, K. Lee, G. Bozoklu and W. Cai, *ACS Nano*, 2008, **2**, 572–578.
74 H.-P. Cong, P. Wang and S.-H. Yu, *Chem. Mater.*, 2013, **25**, 3357–3362.
75 A. Sashu, W. Choi and G. Tae, *Chem. Commun.*, 2012, **48**, 5820–5822.
76 B. Adhikari and A. Banerjee, *Soft Matter*, 2011, **7**, 9259–9266.
77 B. Adhikari, A. Biswas and A. Banerjee, *Langmuir*, 2012, **28**, 1460–1469.
78 Y. Chen, L. Chen, H. Bai and L. Li, *J. Mater. Chem. A*, 2013, **1**, 1992–2001.
79 Z. Sui, Y. Cui, J. Zhu and B. Han, *ACS Appl. Mater. Interfaces*, 2013, **5**, 9172.
80 H. Huang, S. Lu, X. Zhang and Z. Shao, *Soft Matter*, 2012, **8**, 4609–4615.
81 H. Sun, Z. Xu and C. Gao, *Adv. Mater.*, 2013, **25**, 2554–2560.
82 Z. Xu, H. Sun, X. Zhao and C. Gao, *Adv. Mater.*, 2013, **25**, 188–193.
83 Y. Xu, Q. Wu, Y. Sun, H. Bai and G. Shi, *ACS Nano*, 2010, **4**, 7358–7362.
84 S. Ye, J. Feng and P. Wu, *J. Mater. Chem. A*, 2013, **1**, 3495–3502.
85 H. Sehaqui, M. Salajková, Q. Zhou and L. A. Berglund, *Soft Matter*, 2010, **6**, 1824–1832.
86 E. M. Arndt, M. D. Gawryla and D. A. Schiraldi, *J. Mater. Chem.*, 2007, **17**, 3525–3529.
87 X. Xiao, T. Xie and Y.-T. Cheng, *J. Mater. Chem.*, 2010, **20**, 3508–3514.
88 J. Shen, B. Yan, T. Li, Y. Long, N. Li and M. Ye, *Composites, Part A*, 2012, **43**, 1476–1481.
89 R. Liu, S. Liang, X.-Z. Tang, D. Yan, X. Li and Z.-Z. Yu, *J. Mater. Chem.*, 2012, **22**, 14160–14167.
90 Y. Xu, K. Sheng, C. Li and G. Shi, *ACS Nano*, 2010, **4**, 4324–4330.
91 J. Zhao, W. Ren and H.-M. Cheng, *J. Mater. Chem.*, 2012, **22**, 20197–20202.
92 H. Hu, Z. Zhao, W. Wan, Y. Gogotsi and J. Qiu, *Adv. Mater.*, 2013, **25**, 1–5.
93 Z.-S. Wu, A. Winter, L. Chen, Y. Sun, A. Turchanin, X. Feng and K. Müllen, *Adv. Mater.*, 2012, **24**, 5130–5135.
94 Y. Zhao, J. Liu, Y. Hu, H. Cheng, C. Hu, C. Jiang, L. Jiang, A. Cao and L. Qu, *Adv. Mater.*, 2013, **25**, 591–595.
95 J. Che, L. Shen and Y. Xiao, *J. Mater. Chem.*, 2010, **20**, 1722–1727.

96 V. H. Luan, H. N. Tien, L. T. Hoa, N. T. M. Hien, E.-S. Oh, J. Chung, E. J. Kim, W. M. Choi, B.-S. Kong and S. H. Hur, *J. Mater. Chem. A*, 2013, **1**, 208–211.
97 K. Sheng, Y. Xu, C. Li and G. Shi, *New Carbon Mater.*, 2011, **26**, 9–15.
98 W. Chen and L. Yan, *Nanoscale*, 2011, **3**, 3132–3137.
99 W. Chen, S. Li, C. Chen and L. Yan, *Adv. Mater.*, 2011, **23**, 5679–5683.
100 T. Wu, M. Chen, L. Zhang, X. Xu, Y. Liu, J. Yan, W. Wang and J. Gao, *J. Mater. Chem. A*, 2013, **1**, 7612–7621.
101 K. Sheng, Y. Sun, C. Li, W. Yuan and G. Shi, *Sci. Rep.*, 2012, **2**, 247.
102 Y. Li, K. Sheng, W. Yuan and G. Shi, *Chem. Commun.*, 2013, **49**, 291–293.
103 M. F. El-Kady, V. Strong, S. Dubin and R. B. Kaner, *Science*, 2012, **335**, 1326–1330.
104 M. Bryning, D. Milkie and M. Islam, *Adv. Mater.*, 2007, **19**, 661–664.
105 T. Bordjiba, M. Mohamedi and L. H. Dao, *Adv. Mater.*, 2008, **20**, 815–819.
106 S. M. Jung, H. Y. Jung, M. S. Dresselhaus, Y. J. Jung and J. Kong, *Sci. Rep.*, 2012, **2**, 849.
107 L. Tang, Y. Wang, Y. Li, H. Feng, J. Lu and J. Li, *Adv. Funct. Mater.*, 2009, **19**, 2782–2789.
108 L. Guardia, M. J. Fernández-Merino, J. I. Paredes, P. Solís-Fernández, S. Villar-Rodil, A. Martínez-Alonso and J. M. D. Tascón, *Carbon*, 2011, **49**, 1653–1662.
109 M. Lotya, P. J. King, U. Khan, S. De and J. N. Coleman, *ACS Nano*, 2010, **4**, 3155–3162.
110 Z. Peng, Z. Yan, Z. Sun and J. M. Tour, *ACS Nano*, 2011, **5**, 8241–8247.
111 W. Deheer, C. Berger, X. Wu, P. First, E. Conrad, X. Li, T. Li, M. Sprinkle, J. Hass and M. Sadowski, *Solid State Commun.*, 2007, **143**, 92–100.
112 X. Li, W. Cai, J. An, S. Kim, J. Nah, D. Yang, R. Piner, A. Velamakanni, I. Jung, E. Tutuc, S. K. Banerjee, L. Colombo and R. S. Ruoff, *Science*, 2009, **324**, 1312–1314.
113 C. Zhang, L. Fu, N. Liu, M. Liu, Y. Wang and Z. Liu, *Adv. Mater.*, 2011, **23**, 1020–1024.
114 M. J. Allen, V. C. Tung and R. B. Kaner, *Chem. Rev.*, 2010, **110**, 132–145.
115 X. Dong, Y. Cao, J. Wang, M. B. Chan-Park, L. Wang, W. Huang and P. Chen, *RSC Adv.*, 2012, **2**, 4364–4369.
116 A. Leela, M. Reddy, A. Srivastava, S. R. Gowda, H. Gullapalli, M. Dubey and P. M. Ajayan, *ACS Nano*, 2010, **4**, 6337–6342.
117 Z. Luo, S. Lim, Z. Tian, J. Shang, L. Lai, B. MacDonald, C. Fu, Z. Shen, T. Yu and J. Lin, *J. Mater. Chem.*, 2011, **21**, 8038–8044.
118 Z. Chen, W. Ren, L. Gao, B. Liu, S. Pei and H. Cheng, *Nat. Mater.*, 2011, **10**, 424–428.
119 A. C. Ferrari, J. C. Meyer, V. Scardaci, C. Casiraghi, M. Lazzeri, F. Mauri, S. Piscanec, D. Jiang, K. S. Novoselov, S. Roth and A. K. Geim, *Phys. Rev. Lett.*, 2006, **97**, 187401.
120 X. Dong, X. Wang, L. Wang, H. Song, H. Zhang, W. Huang and P. Chen, *ACS Appl. Mater. Interfaces*, 2012, **4**, 3129–3133.
121 X. Dong, X. Wang, J. Wang, H. Song, X. Li, L. Wang, M. B. Chan-Park, C. M. Li and P. Chen, *Carbon*, 2012, **50**, 4865–4870.
122 X. Cao, Y. Shi, W. Shi, G. Lu, X. Huang, Q. Yan, Q. Zhang and H. Zhang, *Small*, 2011, **7**, 3163–3168.
123 H. Bi, F. Huang, J. Liang, Y. Tang, X. Lü, X. Xie and M. Jiang, *J. Mater. Chem.*, 2011, **21**, 17366–17370.
124 X. Xiao, T. E. Beechem, M. T. Brumbach, T. N. Lambert, D. J. Davis, J. R. Michael, C. M. Washburn, J. Wang, S. M. Brozik, D. R. Wheeler, D. B. Burckel and R. Polsky, *ACS Nano*, 2012, **6**, 3573–3579.
125 M. Mecklenburg, A. Schuchardt, Y. K. Mishra, S. Kaps, R. Adelung, A. Lotnyk, L. Kienle and K. Schulte, *Adv. Mater.*, 2012, **24**, 3486–3490.
126 S. H. Lee, H. W. Kim, J. O. Hwang, W. J. Lee, J. Kwon, C. W. Bielawski, R. S. Ruoff and S. O. Kim, *Angew. Chem., Int. Ed.*, 2010, **49**, 10084–10088.
127 M. Hernandez-Guerrero and M. H. Stenzel, *Polym. Chem.*, 2012, **3**, 563–577.
128 H. S. Ahn, J.-W. Jang, M. Seol, J. M. Kim, D.-J. Yun, C. Park, H. Kim, D. H. Youn, J. Y. Kim, G. Park, S. C. Park, J. M. Kim, D. I. Yu, K. Yong, M. H. Kim and J. S. Lee, *Sci. Rep.*, 2013, **3**, 1396.
129 H. S. Ahn, H. Kim, J. M. Kim, S. C. Park, J. M. Kim, J. Kim and M. H. Kim, *Carbon*, 2013, **64**, 27–34.
130 M. Chen, T. Tao, L. Zhang, W. Gao and C. Li, *Chem. Commun.*, 2013, **49**, 1612–1614.
131 Y. J. Shin, Y. Wang, H. Huang, G. Kalon, A. T. S. Wee, Z. Shen, C. S. Bhatia and H. Yang, *Langmuir*, 2010, **26**, 3798–3802.
132 X.-M. Li, D. Reinhoudt and M. Crego-Calama, *Chem. Soc. Rev.*, 2007, **36**, 1350–1368.
133 L. Gao and T. J. McCarthy, *Langmuir*, 2006, **22**, 2966–2967.
134 E. Singh, Z. Chen, F. Houshmand, W. Ren, Y. Peles, H.-M. Cheng and N. Koratkar, *Small*, 2013, **9**, 75–80.
135 Z. Wang, C. Lopez, A. Hirsa and N. Koratkar, *Appl. Phys. Lett.*, 2007, **91**, 023105.
136 A. Chaubey and B. D. Malhotra, *Biosens. Bioelectron.*, 2002, **17**, 441–456.
137 Y. Shao, J. Wang, H. Wu, J. Liu, I. A. Aksay and Y. Lin, *Electroanalysis*, 2010, **22**, 1027–1036.
138 T. Kuila, S. Bose, P. Khanra, A. K. Mishra, N. H. Kim and J. H. Lee, *Biosens. Bioelectron.*, 2011, **26**, 4637–4648.
139 M. Zhou, Y. Zhai and S. Dong, *Anal. Chem.*, 2009, **81**, 5603–5613.
140 H. Chen, M. B. Müller, K. J. Gilmore, G. G. Wallace and D. Li, *Adv. Mater.*, 2008, **20**, 3557–3561.
141 S. Park, N. Mohanty, J. W. Suk, A. Nagaraja, J. An, R. D. Piner, W. Cai, D. R. Dreyer, V. Berry and R. S. Ruoff, *Adv. Mater.*, 2010, **22**, 1736–1740.
142 K. Yang, Ḱ. J. Wan, Ḱ. S. Zhang, Y. Zhang, S. Lee and Z. Liu, *ACS Nano*, 2011, **5**, 516–522.
143 L. Li, Z. Du, S. Liu, Q. Hao, Y. Wang, Q. Li and T. Wang, *Talanta*, 2010, **82**, 1637–1641.
144 J. Zhang, J. Lei, R. Pan, Y. Xue and H. Ju, *Biosens. Bioelectron.*, 2010, **26**, 371–376.

145 X. Zhang, J. Yin, C. Peng, W. Hu, Z. Zhu, W. Li, C. Fan and Q. Huang, *Carbon*, 2011, **49**, 986–995.
146 N. G. Shang, P. Papakonstantinou, M. McMullan, M. Chu, A. Stamboulis, A. Potenza, S. S. Dhesi and H. Marchetto, *Adv. Funct. Mater.*, 2008, **18**, 3506–3514.
147 X.-C. Dong, H. Xu, X.-W. Wang, Y.-X. Huang, M. B. Chan-Park, H. Zhang, L.-H. Wang, W. Huang and P. Chen, *ACS Nano*, 2012, **6**, 3206–3213.
148 J. Zhang, L. Wang, D. Pan, S. Song and C. Fan, *Chem. Commun.*, 2007, 1154–1156.
149 X. Dong, Y. Ma, G. Zhu, Y. Huang, J. Wang, M. B. Chan-Park, L. Wang, W. Huang and P. Chen, *J. Mater. Chem.*, 2012, **22**, 17044–17048.
150 Y. Ding, Y. Wang, L. Su, M. Bellagamba, H. Zhang and Y. Lei, *Biosens. Bioelectron.*, 2010, **26**, 542–548.
151 R. Pasricha, S. Gupta and A. K. Srivastava, *Small*, 2009, **5**, 2253–2259.
152 D. R. Dreyer, H.-P. Jia and C. W. Bielawski, *Angew. Chem., Int. Ed.*, 2010, **49**, 6813–6816.
153 G. Scheuermann and L. Rumi, *J. Am. Chem. Soc.*, 2009, **131**, 8262–8270.
154 F. Schedin, A. K. Geim, S. V Morozov, E. W. Hill, P. Blake, M. I. Katsnelson and K. S. Novoselov, *Nat. Mater.*, 2007, **6**, 652–655.
155 F. Yavari, C. Kritzinger, C. Gaire, L. Song, H. Gulapalli, T. Borca-Tasciuc, P. M. Ajayan and N. Koratkar, *Small*, 2010, **6**, 2535–2538.
156 Y. Dan, Y. Lu, N. J. Kybert, Z. Luo and T. C. Johnson, *Nano Lett.*, 2009, **9**, 1472–1475.
157 F. Yavari, Z. Chen, A. V Thomas, W. Ren, H.-M. Cheng and N. Koratkar, *Sci. Rep.*, 2011, **1**, 166.
158 O. Leenaerts, B. Partoens and F. Peeters, *Phys. Rev. B: Condens. Matter Mater. Phys.*, 2008, **77**, 125416.
159 J. D. Fowler, M. J. Allen, V. C. Tung, Y. Yang, R. B. Kaner and B. H. Weiller, *ACS Nano*, 2009, **3**, 301–306.
160 J. T. Robinson, F. K. Perkins, E. S. Snow, Z. Wei and P. E. Sheehan, *Nano Lett.*, 2008, **8**, 3137–3140.
161 G. Lu, S. Park, K. Yu, R. S. Ruoff, L. E. Ocola, D. Rosenmann, J. Chen and L. Al, *ACS Nano*, 2011, **5**, 1154–1164.
162 G. Lu, L. E. Ocola and J. Chen, *Appl. Phys. Lett.*, 2009, **94**, 083111.
163 W. Wu, Z. Liu, L. a. Jauregui, Q. Yu, R. Pillai, H. Cao, J. Bao, Y. P. Chen and S.-S. Pei, *Sens. Actuators, B*, 2010, **150**, 296–300.
164 P. N. Bartlett and S. K. Ling-Chung, *Sens. Actuators, B*, 1989, **20**, 287–292.
165 J. J. Miasik, A. Hooper and B. C. Tofield, *J. Chem. Soc., Faraday Trans. 2*, 1986, **82**, 1117–1126.
166 T. R. Annunciado, T. H. D. Sydenstricker and S. C. Amico, *Mar. Pollut. Bull.*, 2005, **50**, 1340–1346.
167 M. M. Radetić, D. M. Jocić, P. M. Iovantić, Z. L. J. Petrović and H. F. Thomas, *Environ. Sci. Technol.*, 2003, **37**, 1008–1012.
168 D. Bastani, A. a. Safekordi, A. Alihosseini and V. Taghikhani, *Sep. Purif. Technol.*, 2006, **52**, 295–300.
169 E. U. Kulawardana and D. C. Neckers, *J. Polym. Sci., Part A: Polym. Chem.*, 2010, **48**, 55–62.
170 A. Li, H.-X. Sun, D.-Z. Tan, W.-J. Fan, S.-H. Wen, X.-J. Qing, G.-X. Li, S.-Y. Li and W.-Q. Deng, *Energy Environ. Sci.*, 2011, **4**, 2062–2065.
171 S. Li, S. Tian, C. Du, C. He, C. Cen and Y. Xiong, *Biochem. Eng. J.*, 2010, **162**, 546–551.
172 M. Toyoda and M. Inagaki, *Carbon*, 2000, **38**, 199–210.
173 M. Inagaki, H. Konno, M. Toyoda, K. Moriya and T. Kihara, *Desalination*, 2000, **128**, 213–218.
174 H. Bi, X. Xie, K. Yin, Y. Zhou, S. Wan, L. He, F. Xu, F. Banhart, L. Sun and R. S. Ruoff, *Adv. Funct. Mater.*, 2012, **22**, 4421–4425.
175 X. Dong, J. Chen, Y. Ma, J. Wang, M. B. Chan-Park, X. Liu, L. Wang, W. Huang and P. Chen, *Chem. Commun.*, 2012, **48**, 10660–10662.
176 Y. Liang, Y. Li, H. Wang, J. Zhou, J. Wang, T. Regier and H. Dai, *Nat. Mater.*, 2011, **10**, 780–786.
177 W. Zhou, L. Ge, Z.-G. Chen, F. Liang, H.-Y. Xu, J. Motuzas, A. Julbe and Z. Zhu, *Chem. Mater.*, 2011, **23**, 4193–4198.
178 C. J. Chang, Z.-H. Loh, C. Shi, F. C. Anson and D. G. Nocera, *J. Am. Chem. Soc.*, 2004, **126**, 10013–10020.
179 R. Liu, C. Von Malotki and L. Arnold, *J. Am. Chem. Soc.*, 2011, **133**, 10372–10375.
180 Y.-J. Wang, D. P. Wilkinson and J. Zhang, *Chem. Rev.*, 2011, **111**, 7625–7651.
181 J. Wu, D. Zhang, Y. Wang, Y. Wan and B. Hou, *J. Power Sources*, 2012, **198**, 122–126.
182 H. Wang, Y. Liang, Y. Li and H. Dai, *Angew. Chem., Int. Ed.*, 2011, **50**, 10969–10972.
183 S. Guo and S. Sun, *J. Am. Chem. Soc.*, 2012, **134**, 2492–2495.
184 Y. Liang, H. Wang, J. Zhou, Y. Li, J. Wang, T. Regier and H. Dai, *J. Am. Chem. Soc.*, 2012, **134**, 3517–3523.
185 H. Bai, C. Li and G. Shi, *Adv. Mater.*, 2011, **23**, 1089–1115.
186 T. Maiyalagan, X. Dong, P. Chen and X. Wang, *J. Mater. Chem.*, 2012, **22**, 5286–5290.
187 Z.-S. Wu, S. Yang, Y. Sun, K. Parvez, X. Feng and K. Müllen, *J. Am. Chem. Soc.*, 2012, **134**, 9082–9085.
188 K. Gong, F. Du, Z. Xia, M. Durstock and L. Dai, *Science*, 2009, **323**, 760–764.
189 L. Ren, K. S. Hui and K. N. Hui, *J. Mater. Chem. A*, 2013, **1**, 5689–5694.
190 G.-P. Jin, R. Baron, L. Xiao and R. G. Compton, *J. Nanosci. Nanotechnol.*, 2009, **9**, 2719–2725.
191 N. M. Suleimanov, S. M. Khantimerov, E. F. Kukovitsky and V. L. Matukhin, *J. Solid State Electrochem.*, 2008, **12**, 1021–1023.
192 C. Xu, Y. Hu, J. Rong, S. P. Jiang and Y. Liu, *Electrochem. Commun.*, 2007, **9**, 2009–2012.
193 I. Danaee, M. Jafarian, F. Forouzandeh, F. Gobal and M. Mahjani, *Int. J. Hydrogen Energy*, 2008, **33**, 4367–4376.
194 J. Yang, J. Tan, F. Yang, X. Li, X. Liu and D. Ma, *Electrochem. Commun.*, 2012, **23**, 13–16.
195 G.-P. Jin, Y.-F. Ding and P.-P. Zheng, *J. Power Sources*, 2007, **166**, 80–86.
196 Z. Liu, Z. Li, F. Wang, J. Liu, J. Ji, J. Wang, W. Wang, S. Qin and L. Zhang, *Mater. Lett.*, 2011, **65**, 3396–3398.
197 K. Parvez, S. Yang, Y. Hernandez, A. Winter, A. Turchanin and X. Feng, *ACS Nano*, 2012, **6**, 9541–9550.

198 M. Grätzel, *J. Photochem. Photobiol., C*, 2003, **4**, 145–153.
199 S. Zhang, X. Yang, Y. Numata and L. Han, *Energy Environ. Sci.*, 2013, **6**, 1443–1464.
200 D. Yu, E. Nagelli, F. Du and L. Dai, *J. Phys. Chem. Lett.*, 2010, **1**, 2165–2173.
201 D. W. Zhang, X. D. Li, H. B. Li, S. Chen, Z. Sun, X. J. Yin and S. M. Huang, *Carbon*, 2011, **49**, 5382–5388.
202 H. Choi, H. Kim, S. Hwang, Y. Han and M. Jeon, *J. Mater. Chem.*, 2011, **21**, 7548–7551.
203 J. D. Roy-Mayhew, D. J. Bozym, C. Punckt and I. A. Aksay, *ACS Nano*, 2010, **4**, 6203–6211.
204 W. Hong, Y. Xu, G. Lu, C. Li and G. Shi, *Electrochem. Commun.*, 2008, **10**, 1555–1558.
205 S. Yang, X. Feng, X. Wang and K. Müllen, *Angew. Chem., Int. Ed.*, 2011, **123**, 5451–5455.
206 M. Liang and L. Zhi, *J. Mater. Chem.*, 2009, **19**, 5871–5878.
207 G. Wang, X. Shen, J. Yao and J. Park, *Carbon*, 2009, **47**, 2049–2053.
208 K. Sato, M. Noguchi, A. Demachi, N. Oki and M. Endo, *Science*, 1994, **264**, 556–558.
209 C. Menachem, E. Peled, L. Burstein and Y. Rosenberg, *J. Power Sources*, 1997, **68**, 277–282.
210 J. Gong, H. Wu and Q. Yang, *Carbon*, 1999, **37**, 1409–1416.
211 C. Wan Park, S.-H. Yoon, S. I. Lee and S. M. Oh, *Carbon*, 2000, **38**, 995–1001.
212 Y. Wu, S. Fang and Y. Jiang, *J. Mater. Chem.*, 1998, **8**, 2223–2227.
213 E. Yoo, J. Kim, E. Hosono, H. Zhou, T. Kudo and I. Honma, *Nano Lett.*, 2008, **8**, 2277–2282.
214 G. Derrien, J. Hassoun, S. Panero and B. Scrosati, *Adv. Mater.*, 2007, **19**, 2336–2340.
215 Y. Li, B. Tan and Y. Wu, *Nano Lett.*, 2008, **8**, 265–270.
216 W.-M. Zhang, X.-L. Wu, J.-S. Hu, Y.-G. Guo and L.-J. Wan, *Adv. Funct. Mater.*, 2008, **18**, 3941–3946.
217 C. K. Chan, H. Peng, G. Liu, K. McIlwrath, X. F. Zhang, R. Huggins and Y. Cui, *Nat. Nanotechnol.*, 2008, **3**, 31–35.
218 G. Zhou, D.-W. Wang, F. Li, L. Zhang, N. Li, Z.-S. Wu, L. Wen, G. Q. Lu and H.-M. Cheng, *Chem. Mater.*, 2010, **22**, 5306–5313.
219 J.-G. Ren, Q.-H. Wu, G. Hong, W.-J. Zhang, H. Wu, K. Amine, J. Yang and S.-T. Lee, *Energy Technol.*, 2013, **1**, 77–84.
220 H. Xiang, K. Zhang, G. Ji, J. Y. Lee, C. Zou, X. Chen and J. Wu, *Carbon*, 2011, **49**, 1787–1796.
221 K. Evanoff, A. Magasinski, J. Yang and G. Yushin, *Adv. Energy Mater.*, 2011, **1**, 495–498.
222 B. Lung-Hao Hu, F.-Y. Wu, C.-T. Lin, A. N. Khlobystov and L.-J. Li, *Nat. Commun.*, 2013, **4**, 1687.
223 H. Wang, Y. Yang, Y. Liang, J. T. Robinson, Y. Li, A. Jackson, Y. Cui and H. Dai, *Nano Lett.*, 2011, **11**, 2644–2647.
224 *New battery anode with four times the capacity of conventional materials*, can be found under http://xgsciences.com/releases/new-battery-anode/, 2013.
225 *Cabot Launches First Graphene-Based Additive to Improve Energy Density of Lithium-Ion Batteries*, can be found under http://investor.cabot-corp.com/phoenix.zhtml?c=94559&p=irol-newsArticle&ID=1788701&highlight=, 2013.
226 X. Zhou and Z. Liu, *IOP Conf. Ser.: Mater. Sci. Eng.*, 2011, **18**, 062006.
227 X. Xiao, P. Liu, J. S. Wang, M. W. Verbrugge and M. P. Balogh, *Electrochem. Commun.*, 2011, **13**, 209–212.
228 L. Xiao, D. Wu, S. Han, Y. Huang, S. Li, M. He, F. Zhang and X. Feng, *ACS Appl. Mater. Interfaces*, 2013, **5**, 3764–3769.
229 W. Chen, S. Li, C. Chen and L. Yan, *Adv. Mater.*, 2011, **23**, 5679–5683.
230 H. Ji, L. Zhang, M. Pettes, H. Li and S. Chen, *Nano Lett.*, 2012, **12**, 2446–2451.
231 N. Li, Z. Chen, W. Ren, F. Li and H.-M. Cheng, *Proc. Natl. Acad. Sci. U. S. A.*, 2012, **109**, 17360–17365.
232 A. S. Prakash, P. Manikandan, K. Ramesha, M. Sathiya, J.-M. Tarascon and A. K. Shukla, *Chem. Mater.*, 2010, **22**, 2857–2863.
233 Y. Shi, L. Wen, F. Li and H.-M. Cheng, *J. Power Sources*, 2011, **196**, 8610–8617.
234 H.-G. Jung, M. W. Jang, J. Hassoun, Y.-K. Sun and B. Scrosati, *Nat. Commun.*, 2011, **2**, 516.
235 S. Yang, Y. Gong, Z. Liu, L. Zhan, D. P. Hashim, L. Ma, R. Vajtai and P. M. Ajayan, *Nano Lett.*, 2013, **13**, 1596–1601.
236 Q. Zhao, L. Jiao, W. Peng, H. Gao, J. Yang, Q. Wang, H. Du, L. Li, Z. Qi, Y. Si, Y. Wang and H. Yuan, *J. Power Sources*, 2012, **199**, 350–354.
237 C. V. Subba Reddy, E. H. Walker Jr, S. A. Wicker Sr, Q. L. Williams and R. R. Kalluru, *Curr. Appl. Phys.*, 2009, **9**, 1195–1198.
238 Z. Chen, S. Gao, L. Jiang, M. Wei and K. Wei, *Mater. Chem. Phys.*, 2010, **121**, 254–258.
239 F. Wang, Y. Liu and C. Liu, *Electrochim. Acta*, 2010, **55**, 2662–2666.
240 X. Ren, S. S. Zhang, D. T. Tran and J. Read, *J. Mater. Chem.*, 2011, **21**, 10118–10125.
241 J. Xiao, D. Mei, X. Li, W. Xu, D. Wang, G. L. Graff, W. D. Bennett, Z. Nie, L. V Saraf, I. A. Aksay, J. Liu and J.-G. Zhang, *Nano Lett.*, 2011, **11**, 5071–5078.
242 Z.-L. Wang, D. Xu, J.-J. Xu, L.-L. Zhang and X.-B. Zhang, *Adv. Funct. Mater.*, 2012, **22**, 3699–3705.
243 Y. Wang, Z. Shi, Y. Huang, Y. Ma, C. Wang, M. Chen and Y. Chen, *J. Phys. Chem. C*, 2009, **113**, 13103–13107.
244 C. Liu, Z. Yu, D. Neff, A. Zhamu and B. Z. Jang, *Nano Lett.*, 2010, **10**, 4863–4868.
245 Y. Zhu, S. Murali, M. D. Stoller, K. J. Ganesh, W. Cai, P. J. Ferreira, A. Pirkle, R. M. Wallace, K. Cychosz, M. Thommes, D. Su, E. Stach and R. S. Ruoff, *Science*, 2011, **332**, 1537–1541.
246 A. Mathkar, D. Tozier, P. Cox, P. Ong, C. Galande, K. Balakrishnan, A. Leela, M. Reddy and P. M. Ajayan, *J. Phys. Chem. Lett.*, 2012, **3**, 986–991.
247 C. N. R. Rao, a. K. Sood, K. S. Subrahmanyam and A. Govindaraj, *Angew. Chem., Int. Ed.*, 2009, **48**, 7752–7777.
248 Y. Wang, Y. Wu, Y. Huang, F. Zhang, X. Yang, Y. Ma and Y. Chen, *J. Phys. Chem. C*, 2011, **115**, 23192–23197.
249 H. M. Jeong, J. W. Lee, W. H. Shin, Y. J. Choi, H. J. Shin, J. K. Kang and J. W. Choi, *Nano Lett.*, 2011, **11**, 2472–2477.

250 A. Yu, V. Chabot and J. J. Zhang, *Electrochemical Supercapacitors for Energy Storage and Delivery*, CRC Press, New York, 2013.
251 L. L. Zhang and X. S. Zhao, *Chem. Soc. Rev.*, 2009, **38**, 2520–2531.
252 J. Xia, F. Chen, J. Li and N. Tao, *Nat. Nanotechnol.*, 2009, **4**, 505–509.
253 Z. Xu, Z. Li, C. Holt, X. Tan, H. Wang, B. Amirkhiz, T. Stephenson and D. Mitlin, *J. Phys. Chem. Lett.*, 2012, **3**, 2928–2933.
254 L. Zhang and G. Shi, *J. Phys. Chem. C*, 2011, **115**, 17206–17212.
255 J. Chen, K. Sheng, P. Luo, C. Li and G. Shi, *Adv. Mater.*, 2012, **24**, 4569–4573.
256 W. Wang, S. Guo, M. Penchev, I. Ruiz, K. N. Bozhilov, D. Yan, M. Ozkan and C. S. Ozkan, *Nano Energy*, 2013, **2**, 294–303.
257 S. Ye, J. Feng and P. Wu, *ACS Appl. Mater. Interfaces*, 2013, **5**, 7122–7129.
258 L. L. Zhang, X. Zhao, H. Ji, M. D. Stoller, L. Lai, S. Murali, S. Mcdonnell, B. Cleveger, R. M. Wallace and R. S. Ruoff, *Energy Environ. Sci.*, 2012, **5**, 9618–9625.
259 X. Sun, G. Wang, J.-Y. Hwang and J. Lian, *J. Mater. Chem.*, 2011, **21**, 16581–16588.
260 Y. Wang, A. Yuan and X. Wang, *J. Solid State Electrochem.*, 2007, **12**, 1101–1107.
261 B. E. Conway, V. Birss and J. Wojtowicz, *J. Power Sources*, 1997, **66**, 1–14.
262 X. Xia, J. Tu, Y. Mai, R. Chen, X. Wang, C. Gu and X. Zhao, *Chem. – Eur. J.*, 2011, **17**, 10898–10905.
263 S. Biswas and L. T. Drzal, *Chem. Mater.*, 2010, **22**, 5667–5671.
264 C.-C. Hu and W.-C. Chen, *Electrochim. Acta*, 2004, **49**, 3469–3477.
265 G. Yu, L. Hu, M. Vosgueritchian, H. Wang, X. Xie, J. R. Mcdonough, X. Cui, Y. Cui and Z. Bao, *Nano Lett.*, 2011, **11**, 2905–2911.
266 Y. He, W. Chen, X. Li, Z. Zhang, J. Fu, C. Zhao and E. Xie, *ACS Nano*, 2013, **7**, 174–182.
267 Z.-S. Wu, D.-W. Wang, W. Ren, J. Zhao, G. Zhou, F. Li and H.-M. Cheng, *Adv. Funct. Mater.*, 2010, **20**, 3595–3602.
268 X. Gui, A. Cao, J. Wei, H. Li, Z. Li, L. Fan, K. Wang, H. Zhu and D. Wu, *ACS Nano*, 2010, **4**, 2320–2326.